PCCP

REVIEW

View Article Online
View Journal | View Issue

Cite this: *Phys. Chem. Chem. Phys.*, 2025, **27**, 25204

Bridging MOFs and MXenes: from synthesis to environmental and energy technologies

Muhammad Kashif,[a] Syed Izaz Ali Shah,[a] Salman Khan,[a] Sheraz Ahmad,[a] Muhammad Anwar,[a] Sami Ur Rahman,[a] Shohreh Azizi *[b] and Malik Maaza [b]

Metal–organic frameworks (MOFs) and MXenes have emerged as complementary materials with distinct properties; MOFs offer tunable porosity and functional diversity, while MXenes provide strong electrical conductivity and surface reactivity. Their incorporation into MOF/MXene composites gives excellent performance across various environmental and energy applications. This study focuses on recent breakthroughs in the synthesis of MOF/MXene composites, including hydrothermal, green, self-assembly, and *in situ* approaches. Furthermore, the applications of MXene/MOFs in dye and pharmaceutical degradation are thoroughly discussed. Moreover, the present work also elucidates their applications in hydrogen production and supercapacitor development. The structure–function linkages and material design strategies are examined, giving insight into how the hybrids transcend their specific limits. Finally, key challenges and opportunities are identified to guide future research into scalable and efficient MOF/MXene-based technologies for sustainable environmental and energy systems. This work will contribute predominantly to the ongoing advancement in MXene/MOF hybrid design with applications in various technology sectors, including wastewater treatment, hydrogen production and supercapacitors.

Received 22nd July 2025,
Accepted 13th October 2025

DOI: 10.1039/d5cp02795k

rsc.li/pccp

1. Introduction

Environmental pollution has emerged as a significant global concern in recent years.[1] This growing issue encompasses the contamination of soil, water, and air.[2] Rapid industrialization has significantly increased the production of hazardous organic contaminants, thereby exacerbating pollution in the soil, water and air. Among the primary contributors to environmental pollution, particularly water contamination, are industrial

Muhammad Kashif

Muhammad Kashif is an MPhil student in the Department of Chemistry at Abdul Wali Khan University Mardan, Pakistan. His research focuses on the synthesis and characterization of advanced nanomaterials for hydrogen production, energy storage, water treatment, and environmental remediation. He has developed strong expertise in photocatalytic studies and various material characterization techniques. He is currently pursuing his research under the supervision of Associate Professor Dr Nida Ambreen in the Department of Chemistry.

Syed Izaz Ali Shah

Syed Izaz Ali Shah is an MPhil student in the Department of Chemistry at Abdul Wali Khan University Mardan, Pakistan. His research focuses on the synthesis and characterization of advanced nanomaterials and their applications in environmental sustainability, water treatment, hydrogen production, energy storage, and antibacterial activity. He has developed a strong foundation in material synthesis techniques and spectroscopic analysis under the supervision of Dr Javed Ali Khan, Assistant Professor in the Department of Chemistry.

---

[a] *Department of Chemistry, Abdul Wali Khan University Mardan, Mardan 23200, Pakistan*
[b] *UNESCO-UNISA Africa Chair in Nanoscience and Nanotechnology College of Graduates Studies, University of South Africa, Muckleneuk Ridge, Pretoria, 392, South Africa. E-mail: azizis@unisa.ac.za*

effluents, which include inorganic metal ions, synthetic dyes, aromatic and aliphatic compounds, agricultural residues such as fertilizers and pesticides, pathogenic microbes, and pharmaceutical byproducts.[3,4] Such pollutants pose a significant threat to the global ecosystem, with persistent organic pollutants being particularly concerning due to their longevity and bioaccumulation potential.[5] Historically, dyes were derived from natural sources, such as vegetables, flowers, wood, roots, and insects, until the introduction of synthetic alternatives in 1856.[6] Natural dyes are considered environmentally benign because they degrade easily under sunlight, leaving a minimal ecological footprint. However, the rapid growth of industries such as food processing, plastics, textiles, and cosmetics has escalated the demand for dyes, prompting the widespread adoption of synthetic alternatives to meet this need. Synthetic dyes are crucial to these industries as they offer advantages such as high availability, cost-efficiency, colorfastness, and resistance to light, pH fluctuations, and oxidation. Globally, around 80 000 tons of synthetic dyes are produced each year, yet only about 80% are utilized in the dying process; the remaining 10–15% enter wastewater systems as residual pollutants.[7]

In addition to synthetic dyes, pharmaceutical compounds also contribute significantly to water pollution, posing a serious environmental concern. These pharmaceutical contaminants originate from various sources, including prescription drugs, over-the-counter medications, and veterinary medications. While substances play a crucial role in treating numerous health conditions, their unintended release into the environment poses long-term risks. Pharmaceutical substances fall into several categories, including antiviral (Tamiflu), antidepressant (alprazolam), antiepileptic (carbamazepine), analgesics like naproxen and ibuprofen, antibiotics such as nitrofurantoin, levofloxacin and chloramphenicol (CAP), and hormonal agents like estriol and 17-β estradiol.[8] These chemicals are released into the environment through multiple pathways, including human excretion, livestock waste, hospital effluents, municipal wastewater, improper disposal practices, and industrial discharge from pharmaceutical manufacturing.[9]

Salman Khan

Salman Khan is a prospective PhD student. He completed his MPhil in analytical chemistry at Abdul Wali Khan University Mardan, Pakistan. His research interests include the synthesis and characterization of advanced nanomaterials for environmental remediation, hydrogen production, energy storage, water purification, pyrolysis and biofuel production. He has developed expertise in catalytic materials and analytical characterization techniques. He conducted his research under the supervision of Professor Dr Zahid Hussain in the Department of Chemistry.

Sheraz Ahmad

Sheraz Ahmad is an MPhil student in the Department of Chemistry at Abdul Wali Khan University Mardan, Pakistan. His research focuses on the synthesis and development of advanced nanomaterials for hydrogen production, energy storage, water treatment, and environmental applications. He possesses strong analytical and experimental skills in material characterization and photocatalytic processes. He is currently conducting his research under the supervision of Professor Dr Asad Ali in the Department of Chemistry.

Muhammad Anwar

Muhammad Anwar is an MPhil student in the Department of Chemistry at Abdul Wali Khan University Mardan, Pakistan. His research focuses on the synthesis and application of advanced nanomaterials for environmental remediation, hydrogen production, energy storage, and water treatment. He has developed expertise in nanomaterial synthesis, structural characterization, and photocatalytic studies under the supervision of Dr Javed Ali Khan, Assistant Professor in the Department of Chemistry.

Sami Ur Rahman

Sami Ur Rahman is an MPhil student in the Department of Chemistry at Abdul Wali Khan University Mardan, Pakistan. His research focuses on the design, synthesis, and characterization of advanced nanomaterials for environmental remediation, hydrogen production, energy storage, and water treatment. He has developed strong experimental and analytical skills in material science and photocatalysis. He is currently pursuing his research under the supervision of Professor Dr Niaz Muhammad in the Department of Chemistry.

As a result, untreated human waste containing pharmaceutical residues often leaches into nearby freshwater bodies.[10] One prominent example is the transformation of male fish into female ones due to the development of feminine qualities. Estrogens in the water can also reduce male fertility and may increase the risk of testicular and breast cancer.[11–13] Additionally, anti-cancer drugs found in drinking water are capable of crossing the placental barrier, causing teratogenic and embryotoxic effects. These cytotoxic pharmaceuticals are hazardous for pregnant women due to their potential to disrupt embryonic development.[14–16] Effective removal of organic pollutants from contaminated water is essential for ensuring safety. Water purification involves eliminating contaminants from wastewater to make it suitable for reuse. Traditional treatment methods, such as solvent extraction, ion exchange, chemical precipitation, adsorption, distillation, membrane filtration, and sedimentation, primarily transfer pollutants between phases rather than degrade them, often generating concentrated sludge and incurring high operational costs. In contrast, advanced oxidation processes (AOPs) have emerged as a highly effective method for the removal of organic contaminants. Key AOPs include UV/H_2O_2, UV/S_2O_8, UV/O_3, UV/TiO_2, O_3/H_2O_2, Fe_3O_4/H_2O_2, gamma irradiation, electron beam treatment, and various photocatalytic and electrochemical approaches.

Currently, fossil fuels account for approximately 80% of global energy consumption, although their dominance is gradually declining.[17] However, energy production from fossil fuels contributes substantially to greenhouse gas emissions, particularly CO_2, which accelerates climate change.[18,19] As CO_2 and other greenhouse gas emissions continue to rise, the risks associated with global warming and climate instability are escalating. To mitigate these impacts, a transition toward renewable energy sources and stronger climate policies is essential.[20] For instance, in Hong Kong, direct fossil fuel use in electricity generation and transportation accounts for 48% and 36% respectively, of the estimated 290 000 TJ annual energy consumption.[21] Furthermore, fossil fuel-based energy systems emit a wide range of harmful pollutants, including heavy metals, ashes, radioactivity, SO_x, NO_x, CO_2, *etc.*, at levels far greater than those produced by hydrogen energy systems based on renewable sources.[22] The International Energy Agency (IEA) forecast that CO_2 emissions from the energy sector will rise from 50% in 2030 to 80% in 2050.[23] The pursuit of alternative energy sources has accelerated notably since the 1973 oil crisis, which highlighted the vulnerabilities of fossil fuel dependence.[24] The rapid advancement of the electronics industry and the increasing integration of electronic devices into daily life have spurred the development of clean and renewable energy storage and conversion technologies.[25] As a response to global energy challenges, the efficient storage and conversion of energy has become a defining aspect of technological evolution in the modern world. Among these, supercapacitors are gaining increasing recognition due to their high-power density, long life cycle, and rapid charge discharge capabilities. Supercapacitors are generally classified into electrical double-layer capacitors (EDLCs) and pseudo-capacitors, based on their charge storage mechanisms.[26] EDLCs typically utilize carbon-based electrode materials to form an electrostatic double layer at the electrode–electrolyte interface, enabling energy storage through physical ion adsorption. In contrast, pseudo-capacitors rely on fast and reversible faradaic redox reactions using conducting polymers and metal oxide derivatives to generate electrochemical energy in the presence of applied potential.[27] Therefore, selecting appropriate electrode materials is critical for optimizing supercapacitor performance.

In earlier studies, a wide variety of materials were employed as supercapacitor electrodes, including conducting polymers, metal hydroxides, metal chalcogenides, MXenes, graphene, and various metal oxides. The development of cost-effective materials based on non-precious metals with high product

---

Malik Maaza

Professor Malik Maaza, FRSC, FAAS, OMS, is the Chair of UNESCO-UNISA Africa Chair in Nanosciences and Nanotechnology. He obtained his PhD from Pierre and Marie Curie University (Paris VI) in 1991 and currently serves as a professor at the University of South Africa and a member of iThemba LABS. His research focuses on nanomaterials, photonics, and renewable energy. Professor Maaza has received numerous international awards, including the José Vasconcelos World Award of Education, the ICO Galileo Galilei Award, the UNESCO Spirit of Abdus Salam Award, and South Africa's Order of Mapungubwe. He is a Fellow of the Royal Society of Chemistry and the African Academy of Sciences, with over 600 publications and an h-index of 110.

Shohreh Azizi is a Senior Researcher at the UNESCO UNISA Africa Chair in Nanoscience and Nanotechnology, specializing in biological wastewater treatment and nanotechnology applications. Her work focuses on innovative solutions for industrial and municipal wastewater treatment, acid mine drainage, and environmental sustainability. With extensive research contributions, significant funding, and global collaborations, she continues to drive advancements in sustainable environmental practices.

selectivity and catalytic activity is essential for advancing photocatalysis.[28,29] Metal–organic frameworks (MOFs), which are crystalline porous materials, are synthesized by coordinating metal ions or clusters with organic ligands.[30,31] The growing interest is attributed mainly to their remarkable features, such as high surface area, variable crystalline structures, flexible chemistry, and changeable bandgap.[32,33] Recent studies have demonstrated that the unique layered structure of two-dimensional MXenes enhances photocatalytic hydrogen production and facilitates their integration with other semiconductors as co-catalysts. These materials have been proposed as an effective alternative to noble-metal catalysts, owing to their comparable catalytic properties.[34,35] Among them, titanium carbide (Ti_3C_2) stands out due to its excellent stability, ease of fabrication, enhanced catalytic activity, and the presence of surface functional groups. MXenes possess high electrical conductivity, but their standalone photocatalytic efficiency remains limited. Therefore, they are often employed as a co-catalyst when combined with semiconductors to improve overall system performance. One such example is the incorporation of Ti_3C_2 MXenes with metal organic frameworks (MOFs), forming synergistic composite systems. However, the intrinsic susceptibility of MXene, particularly $Ti_3C_2T_x$, to surface oxidation under ambient conditions remains a major barrier to their practical deployment. Recent advances have demonstrated promising stabilization strategies through both chemical modification and protective coatings. For instance, surface engineering with Al_2O_3 *via* atomic layer deposition has been shown to form a conformal oxide shell that effectively inhibits oxidation without impairing electrical conductivity.[36] Similarly, polymer encapsulation using conductive polymers such as polyaniline and PEDOT has improved both environmental durability and electrochemical performance by passivating surface –OH and –F groups, thereby reducing reactive sites for oxidative attack.[37] Beyond polymer coatings, heterostructure construction has emerged as another visible route: embedding MXene within MOF or carbonaceous frameworks provides physical shielding and additional interfacial stabilization, significantly prolonging structural integrity under humid and oxygen-rich environments.[38] Aqueous processing modifications have also been reported, where optimized pH and antioxidant additives (*e.g.*, ascorbic acid) suppress oxidative degradation during storage and handling.[39] More recently, hybrid coatings combining inorganic oxides with carbon layers have delivered synergistic protection, balancing diffusion barrier properties with enhanced electron transport.[40] Therefore, materials with high electrical conductivity and strong ability to capture and transport photo-induced charge carriers are critical for addressing the inherently low conductivity of MOFs. Ti_3C_2 MXenes fulfil this role effectively due to their outstanding conductivity and structural stability.[41] Furthermore, the interfacial interactions between MOFs and MXenes are key to their composite performance, involving hydrogen bonding, electrostatic forces, and van der Waals interactions between MOF functional groups and MXene surface terminations. Strong interfaces enhance charge transfer, stability, and catalytic activity. Advanced techniques like HRTEM, XPS, and AFM help probe these interactions at the nanoscale, guiding the design of high-performance composites. Despite their promise, MXene-based MOF composites tailored for photocatalytic water splitting remain relatively underexplored. Fig. 1 illustrates different timelines of MXene and MOF composites along with their related publications.

This review presents recent advancements in MOF/MXene composites, emphasizing their synthesis methods, structural features, and multifunctional applications. Particular focus is given to their roles in environmental remediation, sustainable hydrogen production through water splitting and high-performance supercapacitors. The integration of MOFs' high porosity and tunable chemistry with MXenes' excellent conductivity and mechanical strength imparts superior physiochemical characteristics to the composites. By addressing current challenges and future directions, this review offers valuable insights for the rational design of MOF/MXene composites in the energy and environmental fields.

2. Synthesis method

The synthesis of MOF/MXene composites plays a pivotal role in determining their structural integrity, surface functionality, and overall performance in various applications. Several synthesis strategies have been developed to combine the unique properties of MOFs and MXenes effectively. These methods are designed to ensure strong interfacial interactions, uniform dispersion, and optimized composite architectures. Commonly employed techniques include hydrothermal and solvothermal synthesis, which facilitate the growth of MOFs on the MXene surface under controlled temperatures and pressure conditions. *In situ* synthesis enables the direct formation of MOF structures in the presence of MXene, promoting intimate contact at the molecular level. Furthermore, green synthesis methods have gained attention for their environmentally friendly approach, utilizing non-toxic solvents and mild conditions. Additionally, electrostatic attraction methods leverage surface charge interactions to assemble MOF and MXene components effectively. Each of these synthesis approaches offers distinct advantages and challenges (Table 1), which are discussed in detail in the following sections.

2.1 Hydrothermal/solvothermal method

Hydrothermal/solvothermal synthesis methods offer a straightforward approach for fabricating a nanocomposite with controlled morphologies.[44,45] Typically, hydrothermal synthesis promotes the formation of dynamic frameworks, characterized by permanent metal–ligand linkage across the structure.[46,47] Under these conditions, single crystals form within the reactors, guided by the material decomposition rate in hot water under high vapor pressure at elevated temperatures. In contrast, the solvothermal technique uses a solvent other than water to enable material synthesis. While both methods aim to produce high-quality crystalline products, they typically operate

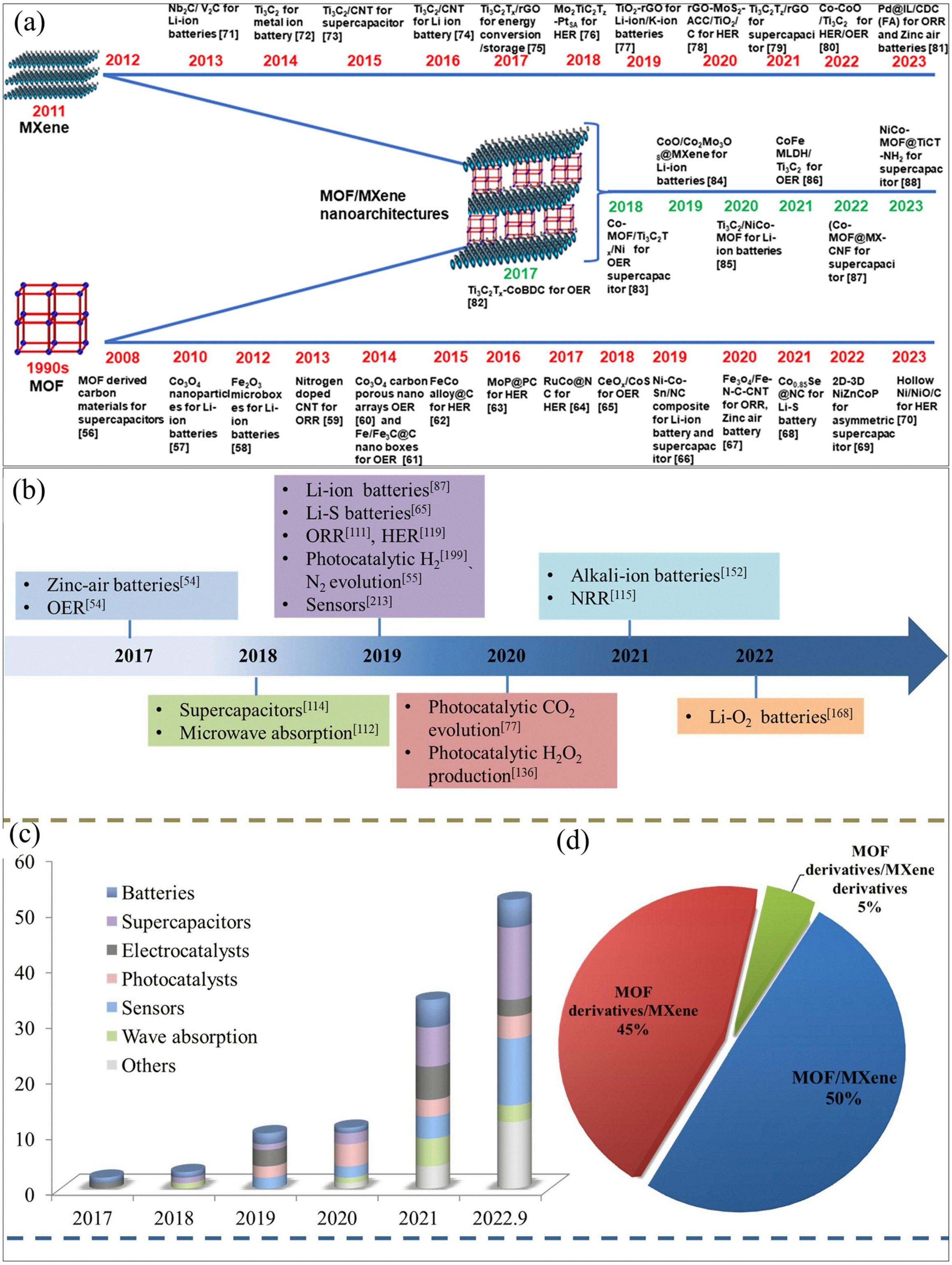

Fig. 1 (a) Chronology of significant advancements in MOF, MXene, and MOF/MXene nanocomposites for electrochemical energy conversion and storage. Reproduced with permission from ref. 42. Copyright 2023, Elsevier, (b) timeline of the initial reports of different MOF/MXene-based composite uses, (c) publications on different uses of MOF/MXene throughout the years and (d) pie chart showing the classification of MOF/MXene-based composites with time. Reproduced with permission from ref. 43. Copyright 2023, Elsevier.

under moderately elevated temperature conditions.[48] These methods typically involve the reaction of metal salts or metal complexes in water or solvents, heated under high pressure and temperatures within an autoclave. Under standard conditions,

Table 1 Summary of different synthesis methods of MXene/MOF composites

Synthesis method	Key features	Advantages	Limitations	Typical applications
Hydrothermal	High temperature/pressure, aqueous-based	Simple, high crystallinity, good morphology control	Long reaction time, energy-intensive	Photocatalysis, adsorption
Solvothermal	Organic solvent-based, high temp/pressure	Wide range of morphologies, high product yield	Solvent toxicity, costly solvents	Catalysis, sensors
In situ	MOF grows in presence of MXene	Strong interface bonding, simple procedure	Requires careful control of conditions	Hybrid materials, energy storage
Green synthesis	Eco-friendly solvents, mild conditions	Environmentally benign, cost-effective	Limited to certain MOFs, lower crystallinity	Catalysis, biomedical
Electrostatic self-assembly	Surface charge-driven assembly	Mild conditions, good dispersion	Less stable under harsh conditions	Photocatalysis, electronics

these reactions proceed over 6 to 48 h, during which disintegration, granulation and crystallization of poorly soluble compounds occur.[49] Among these methods, the solvothermal approach is particularly favored for synthesizing MOFs due to its ability to yield a wide range of morphologies. This method involves reacting an organic ligand with a metal salt in either a solvent mixture or pure organic solvents. Commonly used solvents include acetone, diethyl formamide, methanol, and acetonitrile.[50] When MOF and MXene precursors react under high-temperature solvothermal conditions and self-generated pressure, the process achieves high product yield and remains operationally simple. This technology is especially valuable for controlling the morphology of hybrid materials and fabricating hierarchical architectures.[51] For example, Tian *et al.*[52] fabricated a Ti_3C_2/TiO_2/UiO-66-NH_2 nanocomposite through the solvothermal method (Fig. 2(a)). The process began with stirring the solution for 1 h, after which 2 wt% of TCA was added to the $ZrCl_4$ solution. Subsequently, BDC-NH_2 was added to the suspension, followed by an additional 30 min of stirring. The resulting mixture was transferred into an autoclave and heated at 120 °C for 24 h. After natural cooling, the precipitates were washed with (DMF) to remove unreacted organic ligands, followed by solvent exchange with anhydrous methanol. Finally, the yellow Ti_3C_2/TiO_2/UiO-66-NH_2 product was isolated by centrifugation and dried under vacuum at 80 °C for 12 h. Similarly, Yu *et al.*[53] manufactured the photocatalyst, designated MPA-m/U66N-M *via* a hydrothermal method (Fig. 2(b)). Initially, zirconium tetrachloride ($ZrCl_4$) was completely dissolved in DMF, forming what was referred to as solution A. Once dissolution was complete, the organic molecule MPA-m was added to solution (A), and the mixture was stirred continuously for one hour to ensure proper interaction. In parallel, H_2ATA was dissolved in a separate portion of DMF to form solution (B). Following 30 min of stirring, acetic acid was added to the mixture to facilitate the coordination reaction. The combined solution was subsequently transferred into a reactor

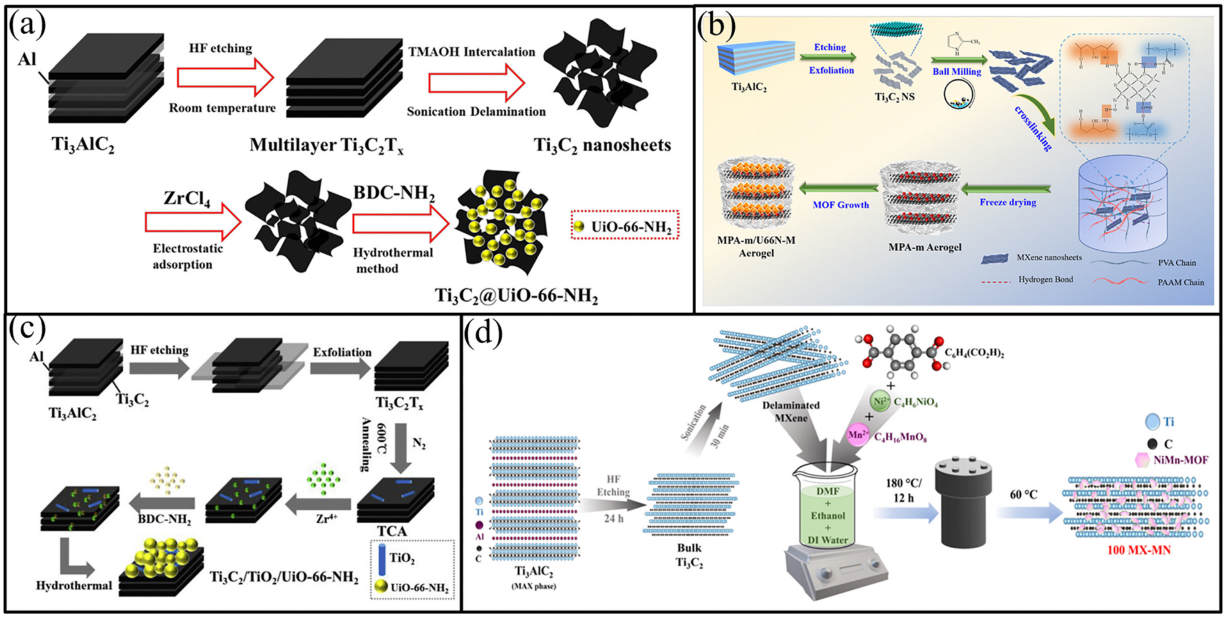

Fig. 2 (a) Schematic depiction of a proposed chemical route for the synthesis of Ti_3C_2/TiO_2/UiO-66-NH_2. Reproduced with permission from ref. 52. Copyright 2019, Elsevier. (b) A demonstration of the MPA-m/U66N-M synthesis method. Reproduced with permission from ref. 53. Copyright 2023, Elsevier. (c) Schematic illustration for preparing Ti_3C_2 nanosheets and the TU series. Reproduced with permission from ref. 54. Copyright 2019, Elsevier. (d) Schematic representation of etching of aluminum from the MAX phase and production of composites. Reproduced with permission from ref. 56. Copyright 2024, Elsevier.

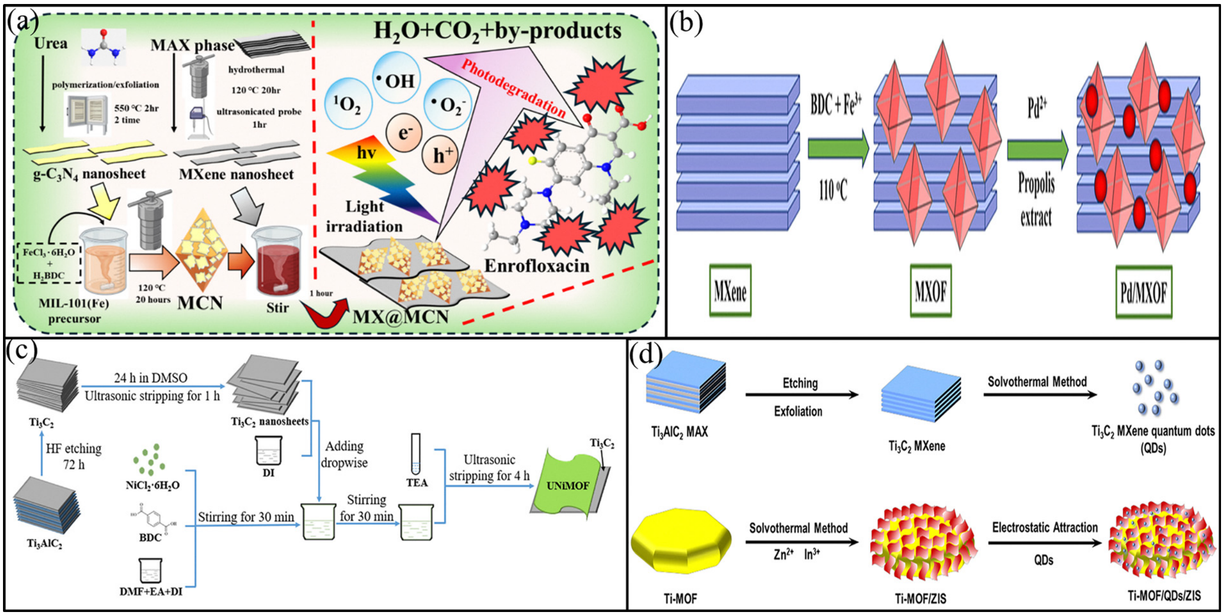

Fig. 3 (a) Description of the production of MX@MCN and its photocatalytic activity to degrade enrofloxacin through light. Reproduced with permission from ref. 58. Copyright 2025, Elsevier. (b) Schematic description of the synthesis of Pd/MXOF photocatalyst. Reproduced with permission from ref. 59. Copyright 2025, Elsevier. (c) Fabrication procedure of the UNiMOF/Ti$_3$C$_2$ composites. Reproduced with permission from ref. 62. Copyright 2021, Elsevier. (d) Schematic representation of the synthesis of *Z*-scheme NH$_2$-MIL-125 (Ti)/Ti$_3$C$_2$ MXene quantum dots ZnIn$_2$S$_4$ composites (Ti-MOF/QDs/ZIS). Reproduced with permission from ref. 63. Copyright 2022, Elsevier.

and subjected to micro-assisted hydrothermal treatment at 120 °C for 40 min under 300 W of microwave radiation. After the reaction, the synthesized product was isolated by centrifugation, followed by repeated washing with methanol and DMF to remove unreacted species. Finally, the purified product was dried under vacuum overnight at 80 °C. In another study, Tian *et al.*[54] synthesized a Ti$_3$C$_2$@UiO-66-NH$_2$ nanocomposite using a hydrothermal technique, as illustrated in Fig. 2(c). Initially, a mixed solution of ZrCl$_4$ in DMF and HCl was prepared, referred to as solution (A). Ti$_3$C$_2$ nanosheets were then added to solution (A), followed by stirring for 1 h to ensure uniform dispersion. In a separate step, BDC was dissolved in DMF to form solution (B), which was then gradually added to solution (A). The combined solution was transferred to an autoclave and subjected to hydrothermal treatment at 120 °C for 24 h. After cooling, the resulting products were collected by centrifugation, thoroughly washed with ethanol and DMF, and then dried at 60 °C for 12 h. Additionally, Yang *et al.*[55] employed a hydrothermal method to synthesize the MX@MIL-125(Ti) nanocomposite. In this synthesis, BDC acted as the organic linker, while the previously prepared Ti$_3$C$_2$ MXene served as the titanium source. To begin, BDC was dissolved in a solvent mixture of DMF and methanol, and the mixture was stirred continuously before the addition of Ti$_3$C$_2$ MXene. Following this, the resulting solution was transferred into an autoclave and heated to 150 °C to initiate the hydrothermal reaction. After 24 h, the suspension was collected, allowed to cool to room temperature, and centrifuged at high speed to separate the solid product by removing the supernatant. To obtain the final MX@MIL-125(Ti) nanocomposite, the precipitate was repeatedly cleaned with fresh methanol and dried. Furthermore, Shalini *et al.*[56] prepared the MN–MX nanocomposite using a hydrothermal approach, as depicted in Fig. 2(d). Initially, the pre-synthesized MX was dispersed in DMF and sonicated for 30 min to ensure proper exfoliation and dispersion. Simultaneously, BDC and ethanol were added to a separate mixture and stirred for 15 min until fully dissolved. Subsequently, [Ni (CH$_3$COO) and [Mn (CH$_3$COO) 2.4H$_2$ 2.4H$_2$O] O] were added into the BDC solution, and stirred for 30 min after complete dissolution. The resulting metal–ligand solution was then poured into the previously sonicated MX solution. To achieve uniform distribution, the combined solution was stirred again for 30 min. The homogeneous solution was then transferred into an autoclave lined with Teflon and heated at 180 °C for 24 h under static conditions. After cooling to room temperature, the resulting light green precipitate was collected and washed with DI water and ethanol. The purified product was then ground using an agate mortar, designated as 25 MX-MN and dried at 60 °C for 12 h.

Liu *et al.*[57] synthesized Ti$_3$C$_2$T$_x$ *vs.* MIL-53(Fe) hybrid materials by adjusting the mass ratio of Ti$_3$C$_2$T$_x$ to MIL-53(Fe) through a practical solvothermal approach. Initially, a predetermined amount of Ti$_3$C$_2$T$_x$ powder was dispersed in DMF using ultrasonic treatment for 2 h to ensure uniform dispersion. Subsequently, FeCl$_3$·6H$_2$O, and H$_2$BDC, were added to the Ti$_3$C$_2$T$_x$ suspension, and the mixture was stirred until a homogenous solution was obtained. The resulting solution was then transferred into an autoclave and subjected to solvothermal treatment at 150 °C for 24 h. Post-synthesis treatment steps were conducted following the same procedure as used for MIL 53(Fe) synthesis. Similarly, Lin *et al.*[58] synthesized MIL-101(Fe)/g-C$_3$N$_4$

nanocomposites (MCN) *via* a hydrothermal method. Initially, the g-C_3N_4 nanosheets were uniformly dispersed in a MIL-101(Fe) precursor solution. The resulting mixture was stirred for 3 h, followed by hydrothermal treatment at 120 °C for 20 h. The obtained brown powder was washed with methanol and vacuum-dried for 12 h at 60 °C. To synthesize the MXene@MIL-101 (Fe)/g-C_3N_4 nanocomposite (MX@MCN) (Fig. 3(a)), the MCN powder was mixed with methanol for 10 min. Subsequently, MXene nanosheets were gradually added to the mixture and stirred for an additional hour. After methanol washing, the resulting solid was freeze-dried for 3 days to yield MX8%@MCN_3 powder.

2.2 Synthesis of the MOF/MXene composite through a green approach

Eslaminejad *et al.*[59] synthesized a Pd/MXOF nanocomposite using an environmentally friendly green approach (Fig. 3(b)). The preparation of MXene/MIL-101(Fe) (MXOF) involves several sequential steps. Initially, MXene powder was ultrasonically dispersed in DMF for 120 min, resulting in what was referred to as mixture 1. Separately, mixture 2 was synthesized by dissolving $FeCl_3·6H_2O$, and H_2BDC, in DMF. These two mixtures were then combined and stirred together for 20 min to initiate the coordination process. The resulting homogenous solution was transferred to an autoclave and heated at 110 °C for one day to facilitate crystallization. To fabricate the Pd/MXOF nanocomposite, the obtained MXOF was first dispersed in ethanol using a bath sonicator. Following this, $Pd(NO_3)_2·2H_2O$ was added into the dispersion. Subsequently, an ethanolic solution of propolis was added dropwise into the suspension under a nitrogen atmosphere. The entire suspension was stirred at ambient temperature for 24 h to ensure uniform deposition and reaction. Finally, the resulting black precipitate was collected, washed with ethanol and water, and dried overnight at 60 °C.

2.3 MOF/MXene synthesis *via* an electrostatic self-assembly approach

Various non-covalent interactions, including electrostatic interaction, pi–pi stacking, and hydrogen bonding, can collectively drive self-assembly, leading to the spontaneous organization of components into an ordered structure.[60,61] For example, Cheng *et al.*[62] employed an electrostatic self-assembly method to synthesize the UNiMOF/Ti_3C_2 nanocomposite (Fig. 3(c)). In the first step, solution A was prepared by dissolving (BDC) in a solvent mixture containing ethanol, DMF, and DI water. Subsequently, $NiCl_2·6H_2O$ was introduced into the solution under vigorous stirring for 30 min to promote precursor interaction. In parallel, suspension B was prepared by dispersing a specific amount of Ti_3C_2 nanosheets in DI water. Suspension B was then gradually added dropwise into solution A while maintaining continuous magnetic stirring. After 30 min of stirring, TEA was rapidly added to the reaction mixture to facilitate nucleation and growth. The mixture was subjected to ultrasonic treatment at 40 Hz for 4 h. After the reaction, the solid product was collected *via* centrifugation to remove the solvent. The precipitate was washed three times with DMF and ethanol, and dried overnight at 90 °C. Liu *et al.*[63] employed an electrostatic attraction approach to prepare a Ti-MOF/QDs/ZIS nanocomposite (Fig. 3(d)). Briefly, Ti-MOF/ZIS was ultrasonically dispersed in distilled water. Following this, the dispersion was purged with nitrogen gas for 60 min to remove dissolved oxygen. A specific amount of Ti dots (QDs) derived from MXene was then added to the oxygen-free dispersion. At pH 7, the MXene QDs are negatively charged, whereas the Ti-MOF/ZIS surface carries a positive charge thereby facilitating electrostatic assembly. The mixture was then stirred continuously at 35 °C for 12 h under a N_2 environment. Finally, the resulting Ti-MOF/QDs/ZIS composite was obtained by filtration, followed by washing the filtered material three times with DI water. The residual solvent was then removed *via* vacuum distillation to obtain the product.

2.4 Synthesis of MOF/MXene through an *in situ* method

Due to spontaneous formation, the bonding at the composite interface tends to be relatively strong. Moreover, this strategy simplifies the synthesis process by eliminating the need for complex, multi-step procedures.[64] Among the commonly employed fabrication methods, *in situ* synthesis remains one of the most widely adopted techniques for composite formation.[65] In the case of MOF/MXene composites, this approach involves adding MXenes into a solution of organic ligands and well-dissolved metal ions. Importantly, this procedure follows the same synthetic route typically used for MOFs themselves. ''The term same synthesis method'' refers to a variety of techniques, including the hydrothermal method, ambient temperature diffusion-assisted interdiffusion reaction and others. Among these, the ambient temperature diffusion method is particularly notable for its simplicity and environmentally friendly conditions, making it both cost-effective and user-friendly.[66] For example, He *et al.*[67] employed an *in situ* synthesis method to fabricate Ti_3C_2/UiO-66-NH_2 composites (Fig. 4(a)). The synthesis began by dissolving $ZrCl_4$ in a solvent of DMF and acetic acid, after which a measured quantity of Ti_3C_2 was added to the solution. After stirring the mixture for 1 h, pre-dissolved BDC-NH_2 in DMF was added, and the combined solution was stirred for an additional 30 min. The resulting mixture was then transferred to an autoclave and heated at 120 °C for 24 h to promote crystallization. After cooling naturally to room temperature, the precipitate was washed with anhydrous methanol and DMF. The yellow precipitates were then vacuum-dried for an entire night at 80 °C and subsequently labeled according to their Ti_3C_2 contents as 5 wt% Ti_3C_2/UiO-66-NH_2, 10 wt% Ti_3C_2/UiO-66-NH_2, 15 wt% Ti_3C_2/UiO-66-NH_2, and 20 wt% Ti_3C_2/UiO-66-NH_2, which are shortened to 1-T/U, 2-T/U, 3-T/U, and 4-T/U, respectively. Far *et al.*[68] prepared a MXene@UiO-66 nanocomposite through an *in situ* method. In this process, UiO-66 crystals were uniformly assembled on the surface of MXene nanosheets (Fig. 4(b)). To begin, $ZrCl_4$ and the TPA ligand were dissolved in DMF at room temperature in the presence of MXene powder, followed by sonication for 15 min. The resulting solution was then transferred into an autoclave and heated at 120 °C for a day. After cooling, the grey products were collected and washed three

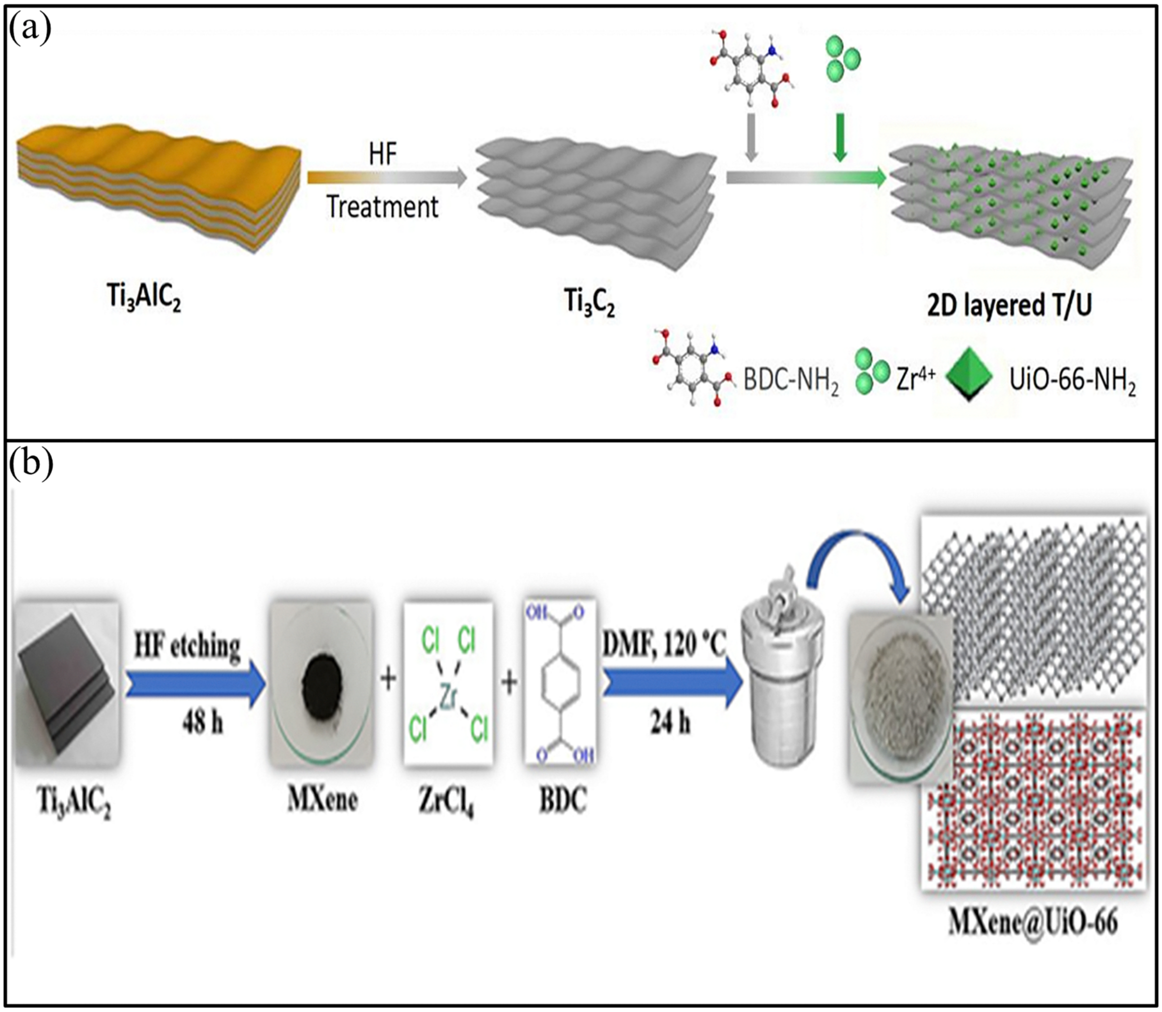

Fig. 4 (a) Schematic diagram for Ti_3C_2 MXene and Ti_3C_2/UiO66NH$_2$ composite preparation. Figure reproduced from ref. 67, which is open access and permits unrestricted use of materials under the terms of the Creative Commons CC-BY. (b) Schematic depiction of the method for synthesizing of the MXene@UiO-66 nanocomposite. Reproduced with permission from ref. 68. Copyright 2024, Elsevier.

times with DI water. Finally, the MXene@UiO-66 was dried at 80 °C for 6 h.

Far *et al.*[69] synthesized the MXOF composite through an *in situ* method involving the formation of the MOF in the presence of MXene. Initially, zinc nitrate and 2-MIM were separately dissolved in methanol in two separate containers. Subsequently, MXene powder was added to the 2-MIM solution and sonicated for 5 min to disperse it. The zinc nitrate solution was then added dropwise to the MXene-containing 2-MIM solution under continuous stirring at 35 °C for 3 h. The resulting product was collected by centrifugation and washed three times with DI water. Finally, the grey powder was subsequently dried for 6 h at 80 °C.

2.5 From lab to industry: MOF scale-up challenges

Scaling up the synthesis of MOF-based and hybrid materials from the laboratory demonstrations to industrial implementation remains a formidable challenge, requiring careful consideration of both economic and technical barriers. At the laboratory scale, solvothermal and hydrothermal methods dominate due to their ability to yield highly crystalline products with tunable structures. However, these techniques often rely on high temperatures, long reaction times, and toxic organic solvents, which significantly hinder large-scale deployment due to environmental, safety, and cost concerns.[70,71] One major bottleneck is the transition to green and scalable synthesis routes such as mechanochemical, electrochemical, and spray-drying strategies, which can minimize solvent usage and reduce energy demand. While mechanochemical synthesis has been demonstrated as a scalable and eco-friendly pathway, reproducibility and control over particle size distribution at industrial throughput remain unresolved.[72] Similarly, continuous flow and microreactor-assisted synthesis offer advantages in automation and uniformity but are yet to be optimized for producing large batches without compromising structural integrity.[73] Another challenge lies in the high cost of ligand and metal precursors, particularly for rare earth or noble metal-based frameworks. Although efforts have been made toward replacing expensive linkers with bio-derived or waste-sourced precursors, such approaches are still underexplored at scale.[74] In addition, maintaining crystallinity, porosity and functionality when shifting from gram-scale to kilogram scale production is nontrivial. For instance defects, inter particle aggregation and morphology inconsistencies frequently appear in called up batches, which directly affect electrochemical or catalytic performance.[75] The integration of conductive dopants or hybridization with carbonaceous nanomaterials introduces further complexity. While doping strategies enhance conductivity and electrochemical stability at small scale, achieving homogenous distribution across kilogram-scale batches is difficult and often results in performance variations.[76] Moreover, the scalability of post-synthetic modifications such as doping, surface functionalization or hybrid composite fabrication remains uncertain due to multi-step processing and high solvent consumption.[77] From an industrial perspective, energy and environmental footprints are also critical. Large scale solvothermal synthesis not only demands substantial thermal energy but also generates significant volumes of solvent waste, which raises issues regarding sustainability and compliance with environmental regulations.[78] Strategies such as solvent recovery, use of water as the reaction medium, and room-temperature synthesis have been proposed, but their applicability across different MOF and hybrid systems is still limited.[79] Finally, the scale-up of electrode integration for energy storage devices poses additional hurdles. Incorporating MOFs or MOF-derived nanostructures into large area electrodes with mechanical robustness, stable interface and long cycling durability requires innovations in processing methods, binder chemistries, and coating technologies.[80] Without advances in these areas, laboratory-scale performance benchmarks may not translate effectively into commercial supercapacitors or batteries. In summary, addressing these challenges demands a holistic approach that combines synthetic innovation, cost-efficient precursors, greener production strategies, and device-level engineering to realize the full potential of MOFs and their hybrids in industrial-scale applications.

3. Applications of MOFs/MXene composites

MOF/MXene composites offer multifunctional capabilities for environmental remediation through efficient pollutant degradation. The enhanced photocatalytic properties support effective hydrogen (H_2) production *via* photocatalysis or electrocatalysis. These materials also exhibit high conductivity and stability, ideal for supercapacitor energy storage. Together, they present a sustainable platform for clean energy and environmental technologies. Furthermore, the photocatalytic performance of MXene-based composites is strongly governed by both surface functionalization and morphological control. Functionalization of the MXene surface with terminal groups (–O, –OH, –F, –S) or heteroatom doping plays a crucial role in tailoring electronic structures, charge separation efficiency, and interfacial interactions with semiconductors partners. For instance, surface engineering through oxygen rich functionalities enhances the density of active sites and promotes stronger interactions with co-catalysts leading to improved redox kinetics.[81] Similarly, heteroatom doping (*e.g.* N, S, P) not only improves visible-light absorption but also modulates the band alignment between MXene and semiconductor photocatalysts, thereby facilitating more efficient charge transfer.[82] Morphology control represents another critical factor in optimizing activity. Exfoliation into ultrathin MXene nanosheets or quantum dots significantly enlarges the specific surface area, offering abundant catalytic sites and shortened diffusion pathways for reactants.[71] Hierarchical or three-dimensional MXene architectures have also been demonstrated to mitigate the common issue of nanosheet restacking, ensuring better accessibility of active sites and enhancing light-harvesting efficiency.[73] Moreover, tailoring the lateral size and thickness of MXene sheets directly influences the charge carrier mobility and surface reaction kinetics providing an effective way to tune the photocatalytic activity toward CO_2 reduction and water splitting.[70] In addition, post-synthetic functionalization with metal cluster or molecular co-catalysts on the MXene surface introduces synthetic effects, where the MXene acts as both an electron mediator and structural scaffold to stabilize highly dispersed active sites. Such hybridization strategies have been reported to significantly boost photocatalytic efficiency while maintaining long term stability under operational conditions.[72] Taken together, surface functionalization and morphology engineering provide powerful levers to tune the photocatalytic activity of MXene-based composites, offering rational design strategies for next-generation catalysts in solar fuel production and environmental remediation.

3.1 Degradation of organic pollutants by the MOF/MXene composite

The degradation of organic pollutants, such as dyes and pharmaceuticals, is crucial for environmental remediation. MOF/MXene composites have emerged as a promising material for photocatalytic degradation of pollutants due to their high surface area, porosity, and conductivity. The synergy between MOFs and MXene composites enhances the photocatalytic activity, leading to improved degradation efficiency of organic pollutants. MOF/MXene composites have shown potential in degrading complex organic pollutants, such as dyes and pharmaceuticals, under various conditions. The photocatalytic activity of MOF/MXene composites can be tailored by adjusting the composition, structure, and morphology.[83] Table 2 summarizes the various pollutant degradations using MXene/MOF composites. Numerous researchers have investigated organic pollutant degradation *via* MXene/MOF composites. For example, Eslaminejad *et al.*[59] synthesized palladium nanoparticles supported on MXene/MOF (Pd/MXOF) *via* a green synthesis route (Fig. 5(a)). The specific surface area of the prepared nanomaterial was 65.874 $m^2\ g^{-1}$. Furthermore, the optical bandgap of the synthesized materials was determined to be 1.79 eV. The prepared nanomaterial was subsequently

Table 2 Summary of the photo-catalytic degradation of organic pollutants by MOF/MXene based composites

			Catalyst properties		Concentration		Reaction conditions					
Pollutant	Photocatalyst	Synthesis method	Band gap (eV)	Surface area (m^2 g^{-1})	Pollutant conc. (mg L^{-1})	Catalyst dose (mg L^{-1})	Light source	Time (min)	pH	Removal (%).	Rate constant (min^{-1})	Ref.
Ciprofloxacin	VCo-MOF@$Ti_3C_2T_x$	Solvothermal	—	150.72	20	5 mg	—	30	5.5	96.1	0.061	88
Ofloxacin (OFL)	Pd/MXOF	Green approach	1.79	65.874	20	0.4	Visible light	30	5.0	100	—	59
Sulfamethoxazole	DA-M100	Solvothermal	2.93	8.8237	20	50 mg	Xenon lamp	60	7.0	92.6	—	86
Tetracycline hydrochloride	La-MOF@MXene (LM-0.1)	Solvent thermal	1.72	58.55	10	10 mg	300 W xenon lamp	120	6.0	92.4	0.00773 min^{-1}	85
Enrofloxacin (ENR)	MX@MCN	Thermal solvent	2.4	825	10	0.25 g L^{-1}	Visible light	60	7.0	99.0	0.069 min^{-1}	58
Tetracycline (TC)	TiCFe	Solvothermal	2.10	17.90	10	10 mg	Xenon lamp	80	—	90.3	0.0286 min^{-1}	57
Tetracycline (TC)	Sn–Bi–MOF/Ti_3C_2	Solvothermal	3.02	145.873	20	40	Xenon lamp	90	11.0	96.2	—	87
Methylene blue (MB)	MXene@UiO-66	Solvothermal *in situ* growth method	4.04	347.28	20	10 mg	Mercury vapor (250 W)	60	—	78.0	—	68
Direct red 31 (DR31)	MXene@UiO-66	Solvothermal *in situ* growth method	4.04	347.28	20	10 mg	Mercury vapor (250 W)	60	—	56.0	—	68
Methylene blue (MB)	UNiMOF/Ti_3C_2	Electrostatic self-assembly process	3.43	27.00	20	50 mg	Xenon lamp	120	6.8	99.49	2.4822 h^{-1}	62
Methyl orange dye	Nd/Dy-MOF@MXene	Solvothermal	2.78	55.21	10	20 mg	Sunlight	30	3.0	93.55	0.0989 min^{-1}	84
Acetone (C_3H_6O)	MXene/MOF aerogel MPA-m/U66N-M	Hydrothermal	2.40	1205	200	0.1 g	Xenon lamp	60	—	95.0	0.052 min^{-1}	53
Methylene blue (MB)	MXOF	*Via in situ* growth	4.99	850.86	20	30 mg	Mercury vapor	60	—	62.0	0.0142 min^{-1}	69
Tetracycline (TC)	BOC/Ti_3C_2	Hydrothermal	2.64	—	20	55 mg	Xenon lamp	120	5.5	81.0	0.05223 mg^{-1} L min^{-1}	89
Tetracycline hydrochloride	NH2-MIL-125(Ti)(TiO_2)/Ti_3C_2 (MT5)	One step solvothermal strategy	—	329	20	0.2 g L^{-1}	Xenon lamp	60	10.5	82.8	0.034 min^{-1}	51
Tetracycline	Ti-MOF/QDs/ZIS	Electrostatic attraction method	2.16	179.8	20	15 mg	Xenon lamp	50	—	96.0	0.0487 min^{-1}	63
Sulfamethazine	Ti-MOF/QDs/ZIS	Electrostatic attraction method	2.16	179.8	30	15 mg	Xenon lamp	40	—	98.0	0.0487 min^{-1}	63
Cr(VI)	Ti_3C_2/UiO-66-NH_2	*In situ* growth	—	—	100	10 mg	Xenon lamp	40	2.0	100.0	0.0871 min^{-1}	67

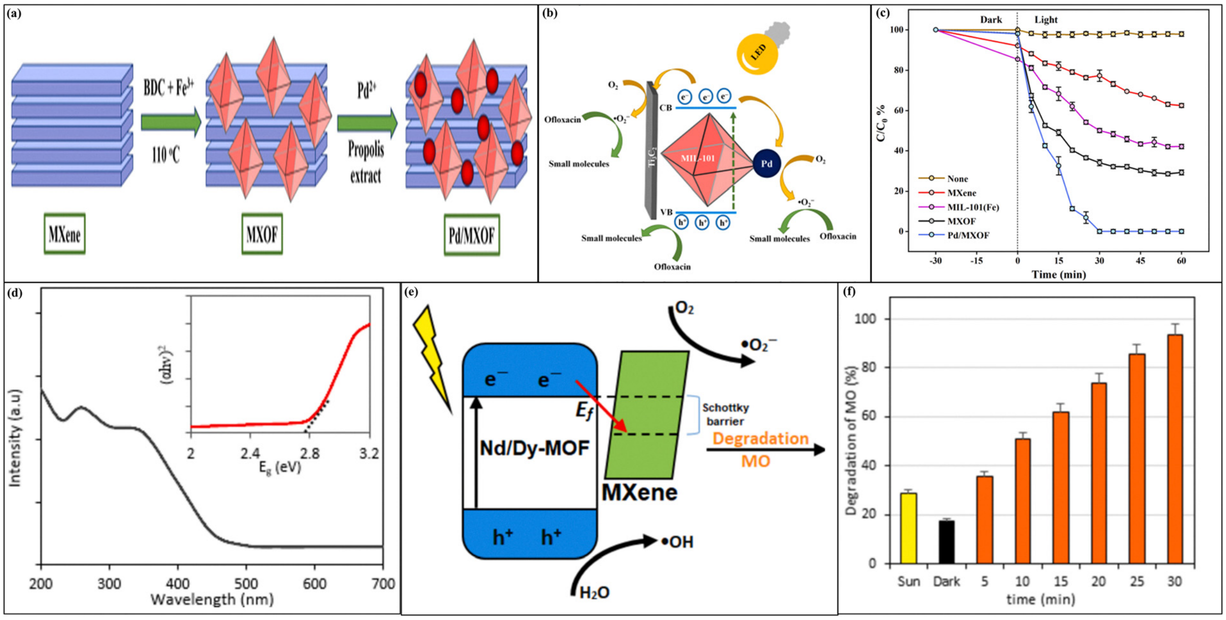

Fig. 5 (a) Synthesis of the Pd/MXOF nanocomposite, (b) degradation of ofloxacin (OFL), and (c) percent degradation of MXene, MOF, MXOF, and Pd/MXOF. Reproduced with permission from ref. 59. Copyright 2024, Elsevier. (d) Bandgap of Nd/Dy-MOF@MXene, (e) mechanism of methyl orange (MO) degradation, and (f) degradation of MO *vs.* time. Reproduced with permission from ref. 84. Copyright 2025, Elsevier.

employed as a visible light-driven photocatalyst for the degradation of ofloxacin (OFL), as shown in Fig. 5(b). The Pd/MXOF nanomaterial shows complete degradation of OFL after 30 min in the presence of visible light irradiation. In contrast, the degradation efficiencies of the pristine MXene, MOF, and MXOF were 70.8, 57.9, and 37.5%, respectively (Fig. 5(c)). In another study, Zairov *et al.*[84] prepared the neodymium/dysprosium-based metal organic framework@MXene (Nd/Dy-MOF@MXene) nanocomposite (NC) by the solvothermal method. The bandgap of the prepared composite was

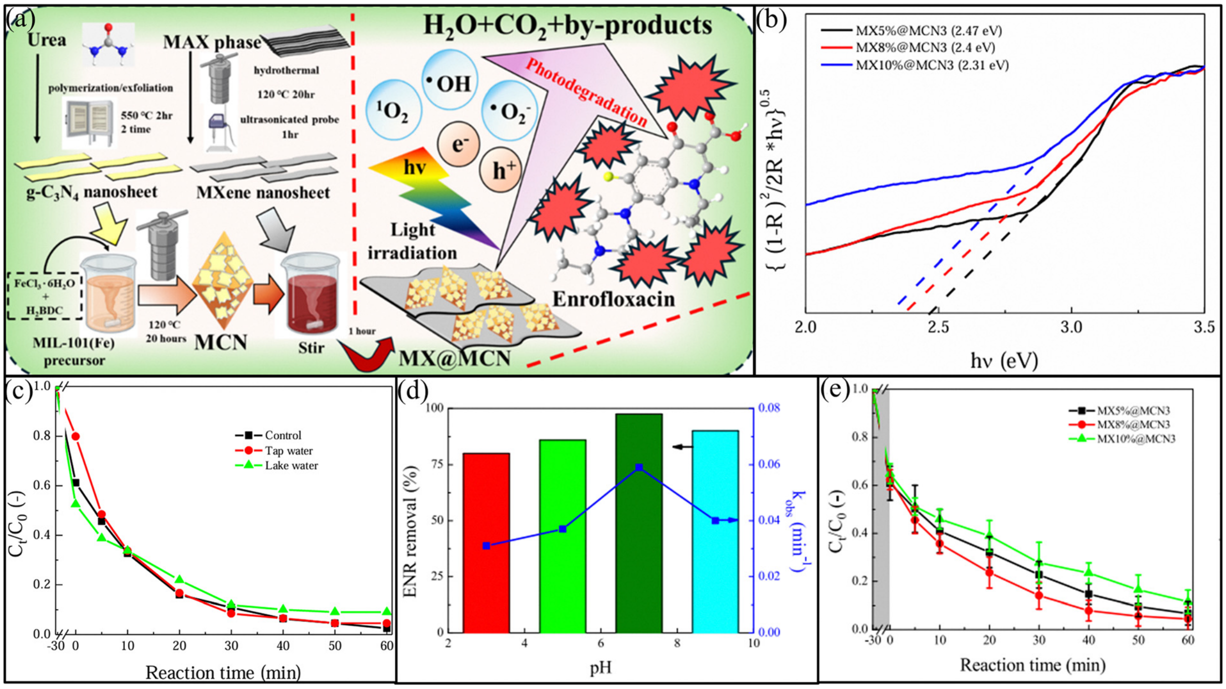

Fig. 6 (a) Synthesis of MX@MCN and its photocatalytic activity against enrofloxacin degradation through light, (b) bandgap of the MX@MCN nanocomposite, (c) impact of the water matrix on the photodegradation of ENR over the MX@MCN photocatalyst when exposed to visible light, (d) pH study of MX@MCN, and (e) photodegradation of enrofloxacin (ENR) over MX@MCN. Reproduced with permission from ref. 58. Copyright 2025, Elsevier.

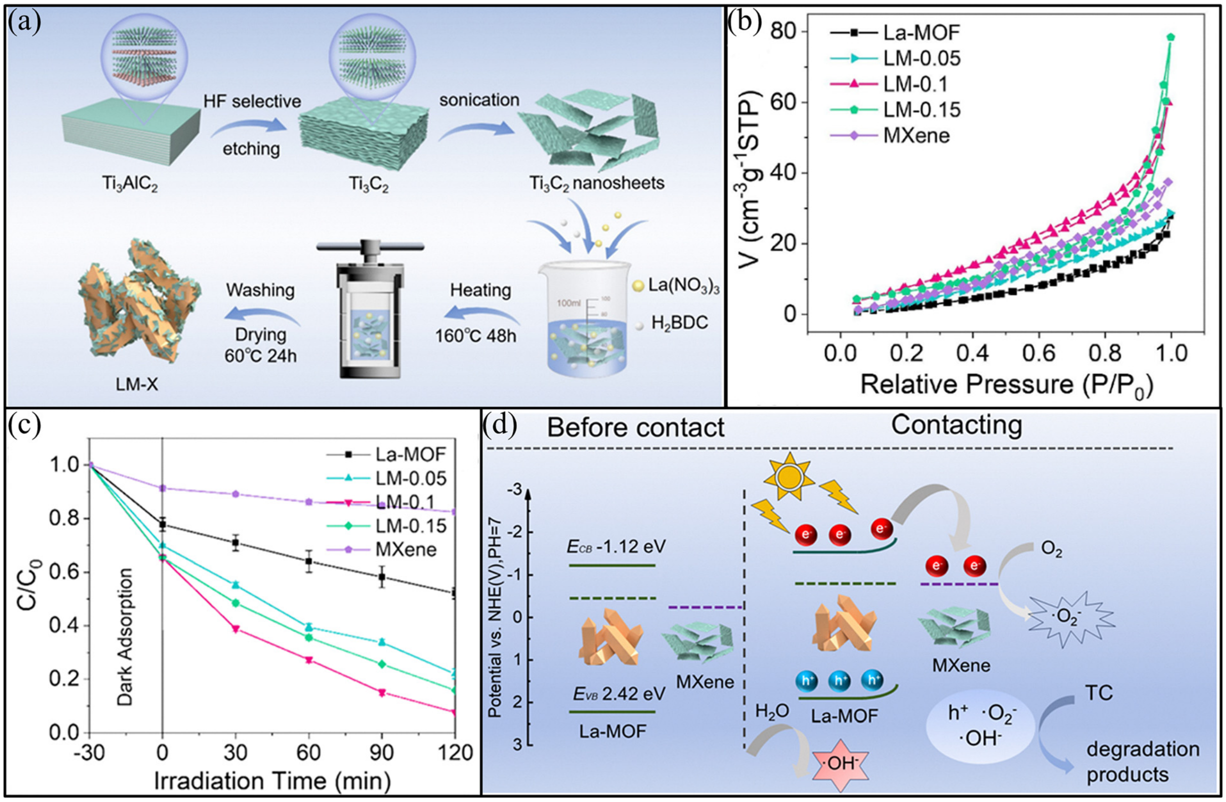

Fig. 7 (a) Schematic representation of the preparation of LM-0.1, (b) N_2 adsorption–desorption isotherms, (c) TC removal with a xenon lamp and (d) possible method for degradation of TC by LM-0.1 under solar light exposure. Reproduced with permission from ref. 85. Copyright 2025, Elsevier.

2.78 eV (Fig. 5(d)). The BET surface area was observed to be 55.21 m^2 g^{-1}. The synthesized NC was used to degrade methyl orange (MO) dye (Fig. 5(e)). The MO degradation was observed to be 16.23% in the absence of light. While the MO degradation reached 27.12% after light irradiation (without a catalyst). Furthermore, the highest degradation of MO was noted to be

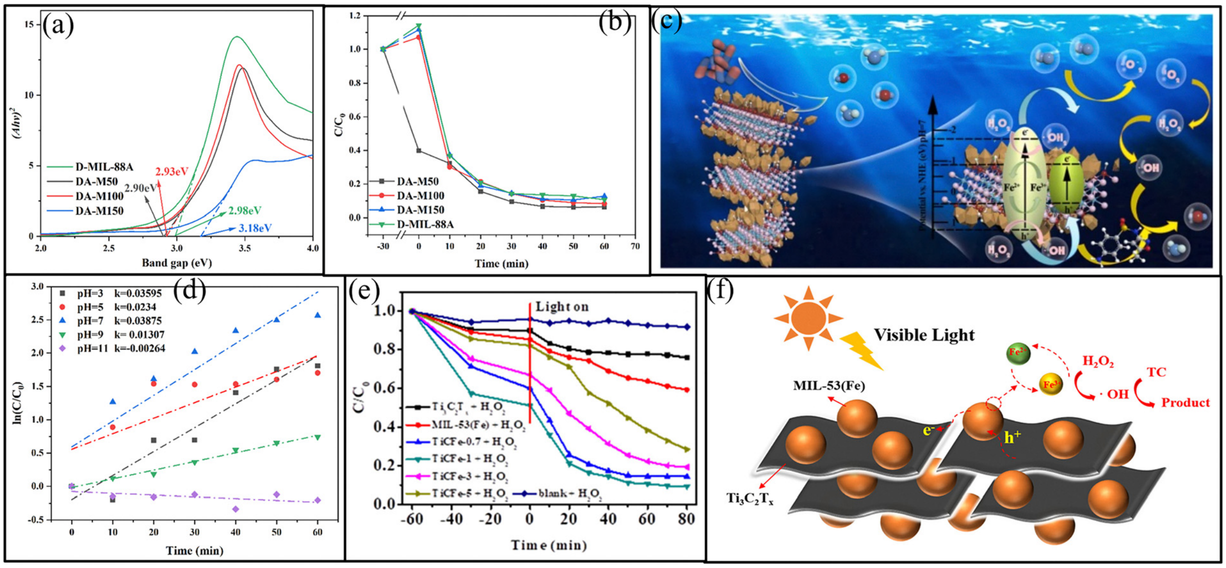

Fig. 8 (a) Bandgap of the photocatalysts, (b) SMZ degradation using different photocatalysts, (c) schematic representation of the DA-M100 adsorption photocatalytic removal method under light conditions, and (d) photocatalytic activity of DA-M100 under different pH conditions. Reproduced with permission from ref. 86 Copyright 2023, Elsevier. (e) Photocatalytic reduction of the tetracycline employing different photocatalysts after 80 min of visible light and (f) schematic representation to degrade TC over the TiCFe-1 composite under visible light. Reproduced with permission from ref. 57. Copyright 2020, Elsevier.

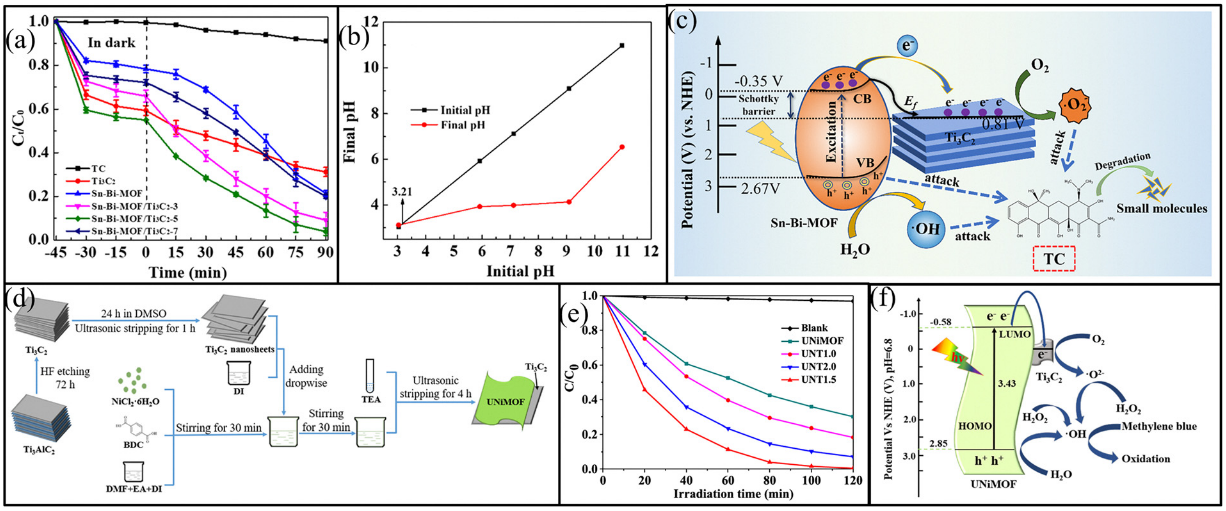

Fig. 9 (a) Tetracycline (TC) degradation of Sn–Bi–MOF/Ti_3C_2, (b) pH effects of Sn–Bi–MOF/Ti_3C_2 on TC, and (c) suggested photocatalytic mechanism of Sn–Bi–MOF/Ti_3C_2. Reproduced with permission from ref. 87. Copyright 2023, Elsevier. (d) Fabrication procedure of the UNiMOF/Ti_3C_2 composites, (e) degradation of MB over the UNiMOF, Ti_3C_2 and UNiMOF/Ti_3C_2 nanocomposite, and (f) the photocatalytic mechanism of UNiMOF towards (MB). Reproduced with permission from ref. 62. Copyright 2021, Elsevier.

93.55% in the presence of light in 30 min, using Nd/Dy-MOF@MXene as a catalyst (Fig. 5(f)).

Similarly, Lin *et al.*[58] synthesized a MX@MCN nanocomposite by a solvothermal method (Fig. 6(a)). The surface area and bandgap of the synthesized catalyst were 825 $m^2\ g^{-1}$ and 2.4 eV, respectively (Fig. 6(b)). The prepared nanocomposite was used for the photocatalytic degradation of enrofloxacin (ENR) as a catalyst. The ENR degradation rate was noted as 99% (Fig. 6(c)) at pH 7 (Fig. 6(d)) in 60 min (Fig. 6(e)), under visible light irradiation.

In addition, Wu *et al.*[85] prepared a La-MOF@MXene (LM-0.1) nanocomposite through a solvent thermal method (Fig. 7(a)). The bandgap of the synthesized material was 1.72 eV. The surface area of the prepared composite was observed to be 58.55 $m^2\ g^{-1}$ (Fig. 7(b)). The prepared materials were used for the photocatalytic degradation of tetracycline HCL. At pH 6 the percent degradation was about 92.4% in 120 min under 300 W Xe lamp irradiation (Fig. 7(c)). A possible method for the degradation of TC by LM-0.1 under solar light exposure was proposed (Fig. 7(d)).

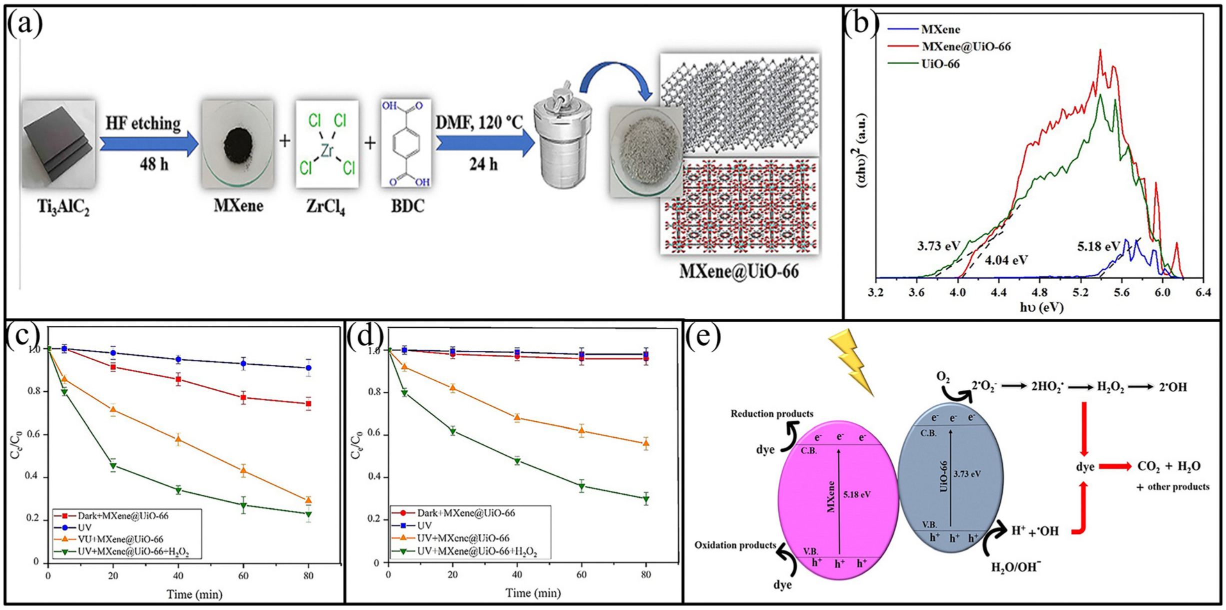

Fig. 10 (a) Schematic representation of the synthesis of the MXene@UiO-66 nanocomposite, (b) the bandgap of MXene, UiO-66, MXene@UiO-66, (c) the degradation performance of the MXene@UiO-66 nanocomposite with MB, (d) the degradation of DR31, and (e) schematic representation of the MB and DR31 degradation mechanism using the MXene@UiO-66 composite. Reproduced with permission from ref. 68. Copyright 2024, Elsevier.

Furthermore, Tan *et al.*[86] synthesized a DA-M100 nanocomposite by a solvent-thermal method. The BET surface area was observed to be 8.8237 $m^2\ g^{-1}$. The bandgap of the obtained nanocomposite was calculated to be 2.93 eV (Fig. 8(a)). The prepared nanocomposite was used as a catalyst for the degradation of sulfamethoxazole. The photocatalyst DA-M100 achieves 70% degradation in 10 min and 92.66% degradation in 60 min at pH 7 (Fig. 8(b)). For comparison, the photocatalytic efficiencies of DA-M50, DA-M150 and DA-MIL-88A (Fe) were also studied. The removal efficiency of sulfamethoxazole was found to be 93.66%, 87.25% and 89.33% using DA-M50, DA-M150 and DA-MIL-88A (Fe), respectively. The excellent removal efficiency of DA-M100 as compared to DA-M50, DA-M150 and DA-MIL-88A was attributed to their low bandgap. The proposed mechanism for the degradation is shown in Fig. 8(c). The potential photocatalytic activity of DA-M100 under various pH conditions is provided in Fig. 8(d). Similarly, Liu *et al.*[57] synthesized a $Ti_3C_2T_x$/MIL-53(Fe) (TiCFe) nanocomposite *via* an *in situ* method. The prepared nanocomposite was used for the removal of tetracycline (TC). The prepared photocatalyst showed an excellent removal rate of 90.3% in 80 min due to the xenon lamp as a light source (Fig. 8(e)). The bandgap and surface area of the prepared photocatalyst were 2.10 eV and 17.90 $m^2\ g^{-1}$, respectively. The proposed catalytic mechanisms of TC are shown in Fig. 8(f).

Cao *et al.*[62] prepared the photocatalyst Sn–Bi–MOF/Ti_3C_2 through the solvothermal method. The synthesized catalyst was used to degrade tetracycline (TC). The TC degrades only 9.9% when there is no catalyst present. The degradation efficiencies of Sn–Bi–MOF and Ti_3C_2 after 90 min of photocatalysis were 79.7% and 69.1%, respectively (Fig. 9(a)). After doping Ti_3C_2 to Sn–Bi–MOF, the degradation of TC reached 96.2% at pH 11 in the presence of a xenon lamp as a light source (Fig. 9(b)). The surface area and bandgap were 145.873 $m^2\ g^{-1}$ and 3.02 eV, respectively. The proposed photocatalytic mechanism of Sn–Bi–MOF/Ti_3C_2 is shown in Fig. 9(c).[87] In addition, Cheng *et al.*[62] synthesized a UNiMOF/Ti_3C_2 photocatalyst by an electrostatic self-assembly process (Fig. 9(d)). The synthesized materials were used to degrade the methylene blue (MB) dye. The

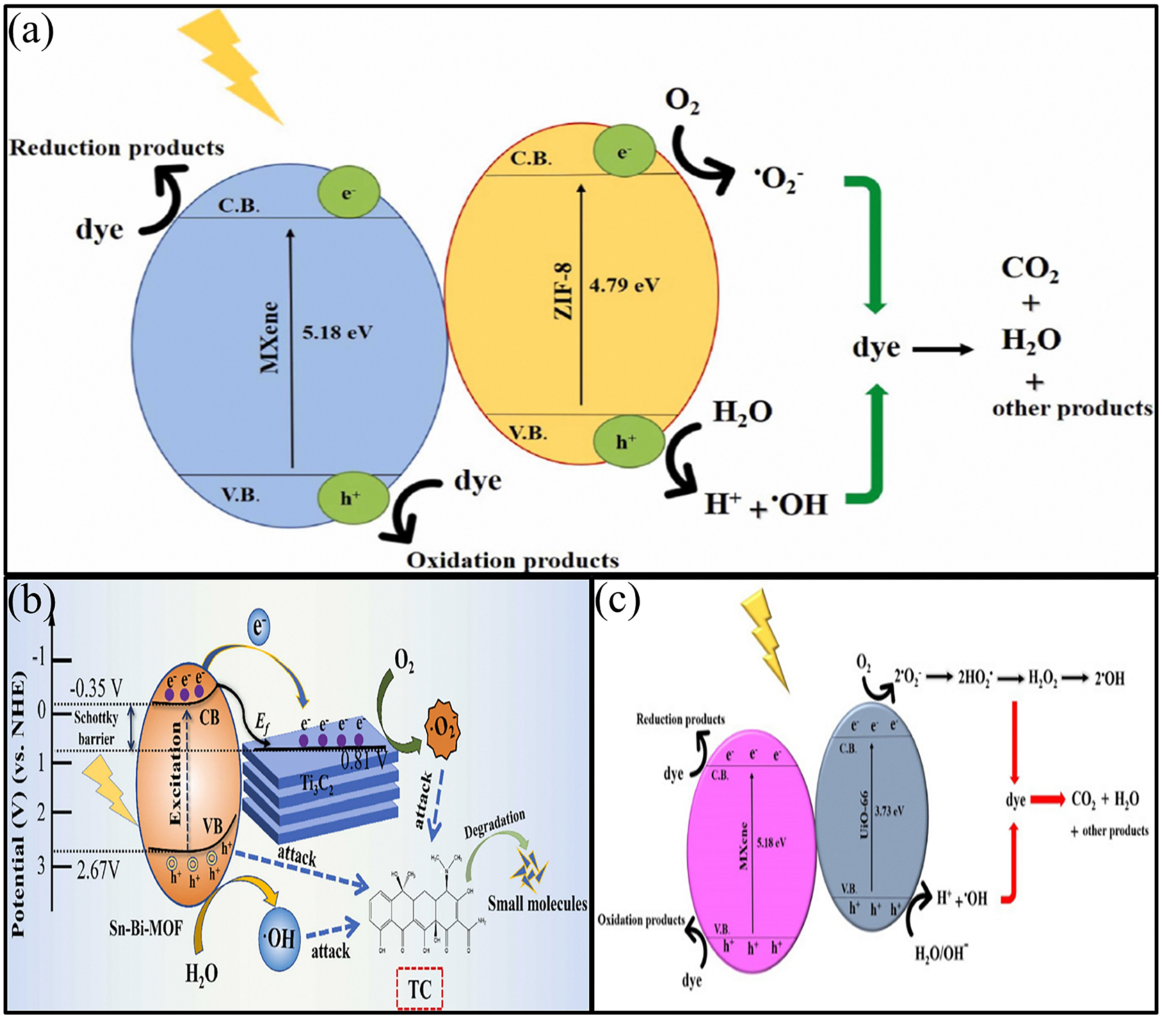

Fig. 11 (a) The degradation method by the MXOF nanocomposite. Reproduced with permission from ref. 69. Copyright 2023, Elsevier. (b) The suggested photocatalytic mechanism in Sn–Bi–MOF/Ti_3C_2.[87] (c) Schematic representation of MB and DR31 degradation mechanism using MXene@UiO-66 nanocomposite. Reproduced with permission from ref. 68. Copyright 2024, Elsevier.

percentage degradation of the synthesized catalyst has an excellent efficiency of 99.49% in 120 min at pH 6.8 in the presence of a xenon lamp as a light source. The degradation efficiency of MB with different catalysts is shown in Fig. 9(e). The synthesized photocatalyst has a bandgap and surface area of 3.43 eV and 27.00 m^2 g^{-1}, respectively. The photocatalytic mechanism of UNiMOF towards MB is shown in Fig. 9(f).

Far *et al.*[68] prepared a MXene@UiO-66 nanocomposite through a solvothermal *in situ* growth method (Fig. 10(a)). The synthesized nanocomposite was utilized for the degradation of MB and direct red 31 (DR31). The surface area and bandgap of the prepared nanocomposite were 347.28 m^2 g^{-1} and 4.04, respectively (Fig. 10(b)). In the presence of mercury vapor (250 W) as a light source, the degradation efficiency of MB (Fig. 10(c)) and DR31 (Fig. 10(d)) was 78% and 56% within 60 min, respectively. The proposed mechanism of photodegradation is shown in Fig. 10(e).

3.1.1 Mechanisms of degradation by MOF/MXene composites. The photocatalytic degradation of organic contaminants using MOF/MXene composites is illustrated in Fig. 11(a). Photocatalytic studies have shown that the MOF/MXene composite absorbs light and energy, resulting in the excitation of electrons and the formation of electron–hole pairs (e^-, h^+).[90,91] The migration of excited electrons through the conduction band (CB) of MOFs and MXene suppresses e^-, h^+ recombination, thereby enhancing radicals' generation and improving the photodegradation efficiency. The generation of reactive radicals primarily depends on the presence of photoexcited electrons (e^-) and holes (h^+). Specifically, when the photoinduced h^+ interact with water molecules, they produce proton and hydroxyl radicals $^{\bullet}OH$, while concurrently converting molecular oxygen into superoxide radicals. The superoxide radicals then react with protons to form hydroperoxyl radicals, which under specific conditions lead to the formation of hydrogen peroxide. Subsequently, hydrogen peroxide decomposes to release additional molecular oxygen and generate more $^{\bullet}OH$, enhancing the oxidative environment. The self-propagating cycle amplifies the radical concentration, thereby enabling the degradation of dye molecules into non-toxic byproducts.[83] The e^- transport mechanism within the Sn–Bi–MOF/Ti_3C_2 heterostructure is well-aligned with the principles of a Schottky junction. Ti_3C_2 acting as a conductive substrate forms a Schottky barrier at its interface with semiconductors.[92] Upon illumination, electrons in the valence band (VB) of the Sn–Bi–MOF catalyst become photoexcited to the CB, leaving h^+ in the VB. The high conductivity of Ti_3C_2 facilitates the rapid migration of electrons from the Sn–Bi–MOF CB to its own structure. Over time, the accumulation of electrons in Ti_3C_2 and h^+ in the VB of Sn–Bi–MOF leads to the formation of a space-charge layer at the interface, constituting a Schottky barrier that effectively traps electrons and prevents their recombination.[93] This mechanism significantly extends the lifetime of photogenerated charge carriers. Simultaneously, electrons on the Ti_3C_2 surface react with oxygen molecules in the electrolyte to generate superoxide radicals ($O_2^{\bullet -}$), while the h^+ in the Sn–Bi–MOF VB oxidize water to form hydroxyl radicals, both of which contribute to the degradation of tetracycline (TC) into smaller, less harmful

Table 3 Summary of the photo-catalytic hydrogen production

				Reaction conditions						
Catalyst	Co-catalyst	Bandgap (eV)	Surface area (m^2 g^{-1})	Catalyst dosage (mg)	Light source	Time (min)	Sacrificial agents	Hydrogen production (μmol g^{-1} h^{-1})	Apparent quantum yield (AQY)	Ref.
Ti_3C_2@MIL-NH_2	Ti_3C_2	2.40	69.2	70	300 W Xenon arc lamp	180	0.3 mL TEOA	4383.1	3.140%	104
Co-ZIF-9/Ti_3C_2	—	—	53.0	50	300 W Xenon lamp	—	Na_2S (0.1 M)/Na_2SO_3 (0.5 M)	3538.5	4.8% 420 nm	105
UZT/CFMX	MX or CFMX	2.82	371.9	—	Xenon lamp	—	TEOA	2187	—	101
Ti-MOF/QDs/ZIS	—	2.16	179.8	25	Xenon lamp	—	0.35 M Na_2S and 0.25 M Na_2SO_3	2931.9	—	63
TiO_2–Ti_3C_2–CoS_x	CoS_x and Ti_3C_2	—	—	20	300 W Xenon lamp	—	Methanol	950	—	106
Ti_3C_2/TiO_2/UiO-66-NH_2	TCA	2.75	987.5	20	300 W Xenon lamp	—	0.1 M Na_2S and 0.1 M Na_2SO_3	1980	—	52
TT/CuTMOF	—	1.74	—	10	300 W Xenon lamp	360	TEOA	19 060	—	107
Ti_3C_2/UiO-66-NH_2 (TU10)	—	2.67	984	20	350 W Xenon lamp	—	0.1 M Na_2S and 0.1 M Na_2SO_3	204	—	54
Ni-MOF/CN/TC	Ti_3C_2 (TC)	2.1	—	5	Solar light (1.5AM_0)	3 h	TEOA	1044.46	—	100
TiO_2/Ti_3C_2–TiC/CZUNH	—	—	348.29	—	Visible light	60 min	Methanol	570	—	108
TCs/Cu-PMOF	—	1.73	20.3	10	300 W Xenon lamp	360	Triethanolamine	1690	—	109

molecules. The suggested photocatalytic mechanisms of the Sn–Bi–MOF/Ti_3C_2 system are depicted in Fig. 11(b). Upon light radiation, the semiconductor photocatalyst absorbs photons with energy equal to or greater than its bandgap, promoting electrons from the VB to the CB, and generating h^+ in the VB (eqn (1)). These photogenerated h^+ oxidize water molecules adsorbed on the catalyst surface, producing reactive $^{\bullet}OH$ and protons (eqn (2)). In addition, hydrogen peroxide present in the reaction can accept CB electrons, producing $^{\bullet}OH$ and hydroxide ions (eqn (3)). Photogenerated h^+ may also oxidize surface hydroxyl ions, further contributing to $^{\bullet}OH$ generation (eqn (4)). Meanwhile, dissolved oxygen molecules capture CB electrons to form the superoxide anion radicals ($O_2^{\bullet-}$) (eqn (5)). These superoxide radicals subsequently react with protons to form hydroperoxyl radicals ($^{\bullet}OOH$) (eqn (6)). Hydroperoxyl radicals can further react with each other to yield hydrogen peroxide and molecular oxygen (eqn (7)). Finally, the reactive oxygen species ($^{\bullet}OH$, $O_2^{\bullet-}$, $^{\bullet}OOH$) and photogenerated h^+ degrade organic contaminants into harmless mineralized products like carbon dioxide and water (eqn (8)).[94]

$$\mathrm{Sc} + h\nu \rightarrow h^+_{VB} + e^-_{CB} \tag{1}$$

$$H_2O + h^+_{VB} \rightarrow {}^{\bullet}OH + H^+ \tag{2}$$

$$H_2O_2 + e^-_{CB} \rightarrow {}^{\bullet}OH + OH^- \tag{3}$$

$$OH^- + h^+_{VB} \rightarrow {}^{\bullet}OH \tag{4}$$

$$O_2 + e^-_{CB} \rightarrow O_2^{\bullet-} \tag{5}$$

$$O_2^{\bullet-} + H^+ \rightarrow {}^{\bullet}OOH \tag{6}$$

$$2{}^{\bullet}OOH \rightarrow H_2O_2 + O_2 \tag{7}$$

$$\begin{aligned}{}^{\bullet}OH/O_2^{\bullet-}/h^+ + \text{organic pollutants} \rightarrow \text{degradation products} +\\ CO_2 + H_2O\end{aligned} \tag{8}$$

When irradiated with light, the MXene@UiO-66 nanocomposite generates e^-, h^+ pairs, with an e^- in the CB and a hole in the VB. Electrons excited in the CB of MXene can transfer to the CB of UiO-66 due to their favorable alignment. Additionally, h^+ are transferred from the VB of UiO-66 to the VB of the MXene due to the higher CB edge potential of MXene relative to UiO-66.[95] Water molecules present in the DR31 and MB dye solutions can be oxidized *via* photogenerated species in the CB to produce $^{\bullet}OH$. Additionally, CB electrons can reduce ambient oxygen to produce superoxide radicals (O_2^-). These reactive species, including superoxide radicals and $^{\bullet}OH$, synergistically degrade the MB and DR31 dye molecules into smaller, less harmful compounds.[96] The internal electric field formed at the MXene–UiO-66 interface, coupled with charge carrier cycling, effectively suppresses the recombination of photogenerated e^-, h^+ pairs. As a result, the overall photocatalytic degradation efficiency of the MXene@UiO-66 nanocomposite is significantly enhanced. The proposed photocatalytic degradation mechanism facilitated by MXene@UiO-66 is illustrated in Fig. 11(c).

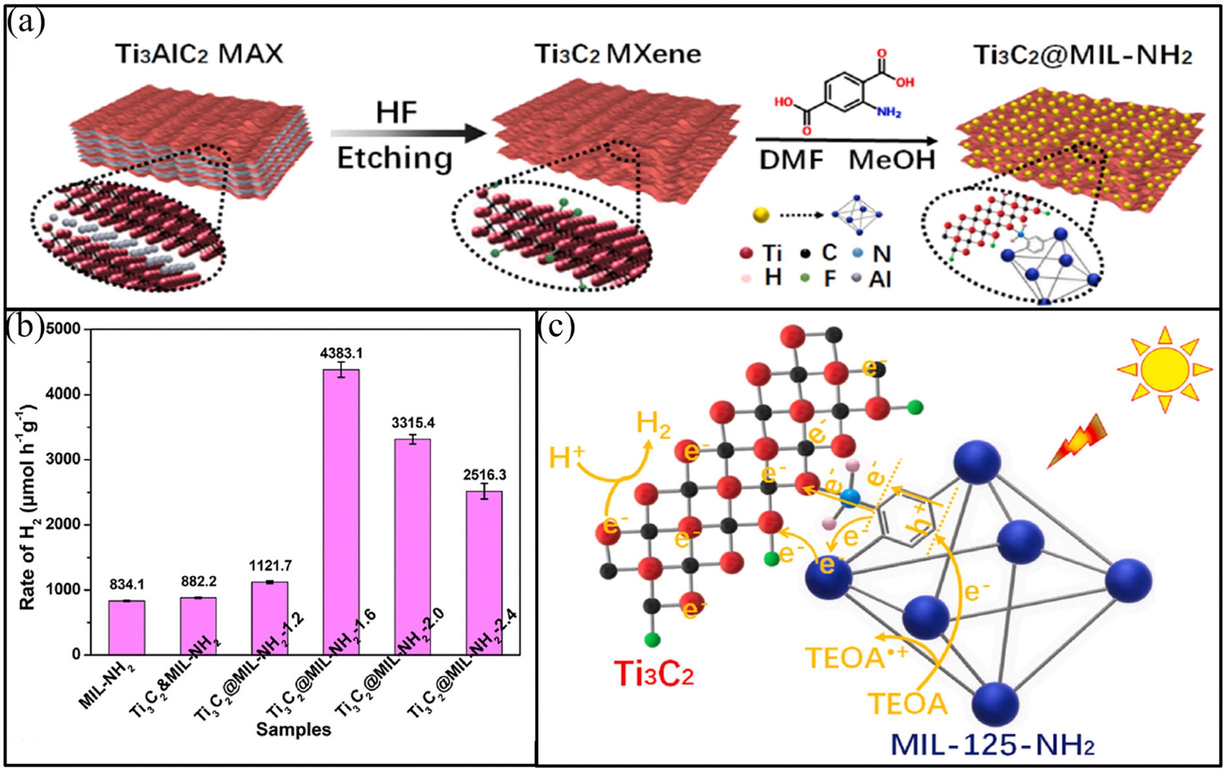

Fig. 12 (a) Schematic preparation process of Ti_3C_2@MIL-NH_2, (b) H_2 production over the MIL-NH_2, Ti_3C_2&MIL-NH_2 and Ti_3C_2@MIL-NH_2 composites, and (c) mechanism for H_2 production over the Ti_3C_2@MIL-NH_2 composite. Reproduced with permission from ref. 104. Copyright 2021, Elsevier.

3.2 Hydrogen production by MOF/MXene composites

Hydrogen can be used as a clean energy carrier, offering a potential alternative to fossil fuels and reducing greenhouse gas emissions. Hydrogen production through photocatalytic water splitting is a promising approach for producing clean and sustainable energy. MOF/MXene composites have emerged as promising materials for photocatalytic hydrogen production due to their enhanced charge separation and improved light absorption.[97] The combination of MOFs and MXene optimizes the electronic structure, reducing the kinetic energy barriers and improving catalytic performance.[98] Experimental studies have demonstrated the superior hydrogen evolution performance of the MOF/MXene composites, but the underlying atomic-level origin of this activity requires further clarification. Recent density functional theory (DFT) investigations provide valuable mechanistic insights into how interfacial electronic interactions dictate catalytic efficiency. The intimate electronic coupling at the MOF/MXene interface plays a decisive role in regulating efficiency for hydrogen evolution, and DFT calculations have been instrumental in clarifying the underlying atomic-level processes. Recent work on 2D MOF-$Ti_3C_2T_x$ Schottky-type heterojunctions has revealed strong interfacial charge redistribution, the rate of photogenerated carriers and the simultaneous shift of the metal-center d-band toward optimal H^+ binding.[99] In Ni-MOF/g-C_3N_4/Ti_3C_2 hybrids, DFT showed that electrons preferentially flow from MXene into Ni nodes, thereby reducing ΔG-H^+ and creating a thermodynamically more favorable landscape for the Volmer stem.[100] Beyond charge transfer, interfacial coordination and defect chemistry introduce additional active motifs. Coordination bonding between MXene surface terminations (–O, –OH) and MOF secondary building units generates low-coordination metal centers that exhibit near-thermoneutral adsorption energies for H^+, providing kinetically accessible pathways for both Volmer and Heyrovsky/Tafel processes.[101] Similarly, bimetallic MOF/MXene composites, such as MIL-100ZIF-7/MXene, display enhanced stabilization of reaction intermediates due to interfacial electronic synergy; a conclusion reinforced by both experimental HER activity and supporting DFT calculations.[102] Complementary reviews also highlight that Schottky-junction behavior, widely observed in MOF/MXene heterostructures, establishes internal fields that direct charge flow across the interface and prolong carrier lifetime, ultimately enhancing hydrogen evolution efficiency.[103] Collectively, these computational studies converge on a unifying mechanism: (i) directional charge transfer at the MOF/MXene interface modulates the electronic structure of the catalytic sites, (ii) defect and coordination-driven low-coordination metal centers offer optimized hydrogen adsorption, and (iii) Schottky-type alignment suppresses recombination and accelerates proton–electron coupling. These atomic-level insights explain the superior hydrogen evolution performance consistently observed in

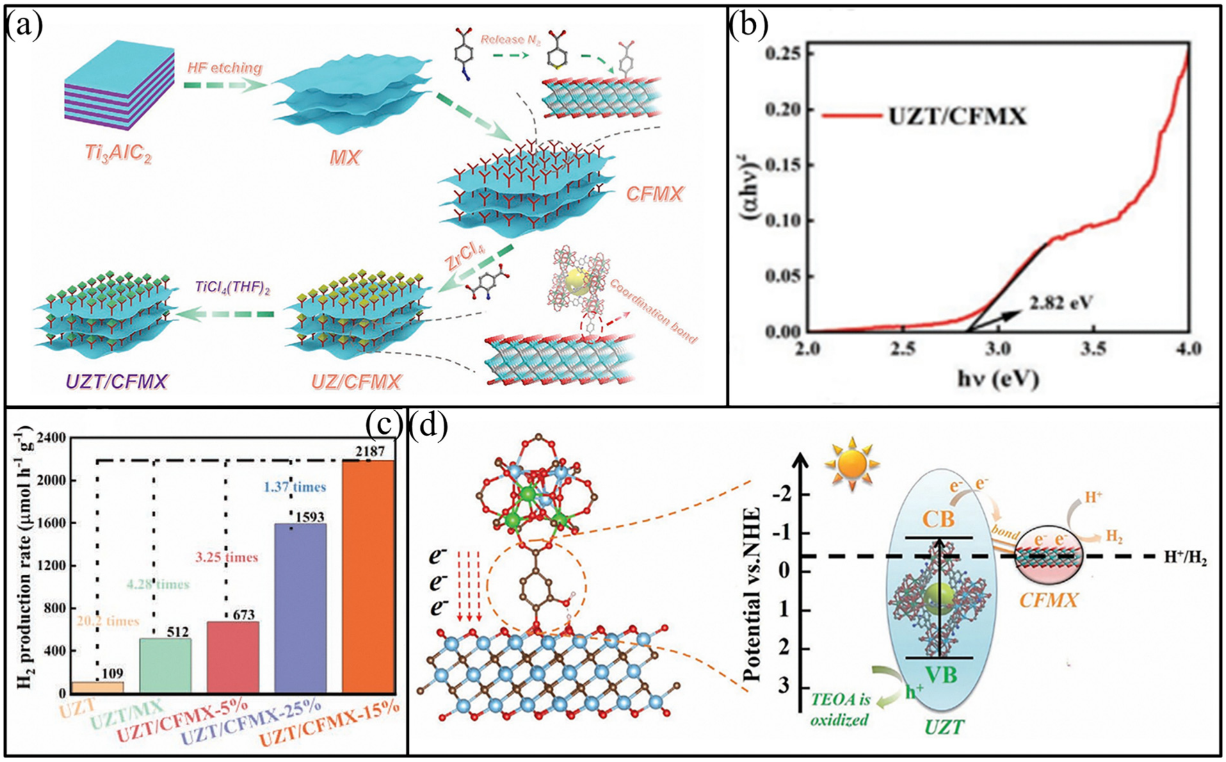

Fig. 13 (a) Schematic illustration of the construction of the UZT/CFMX heterostructure, (b) bandgap of UZT/CFMX, (c) H_2 production of UZT, UZT/MX, UZT/CFMX-5%, UZT/CFMX-15%, and UZT/CFMX-25%, and (d) photocatalytic water splitting mechanism for UZT/CFMX. Reproduced with permission from ref. 101. Copyright 2022, open access CC BY 4.0.

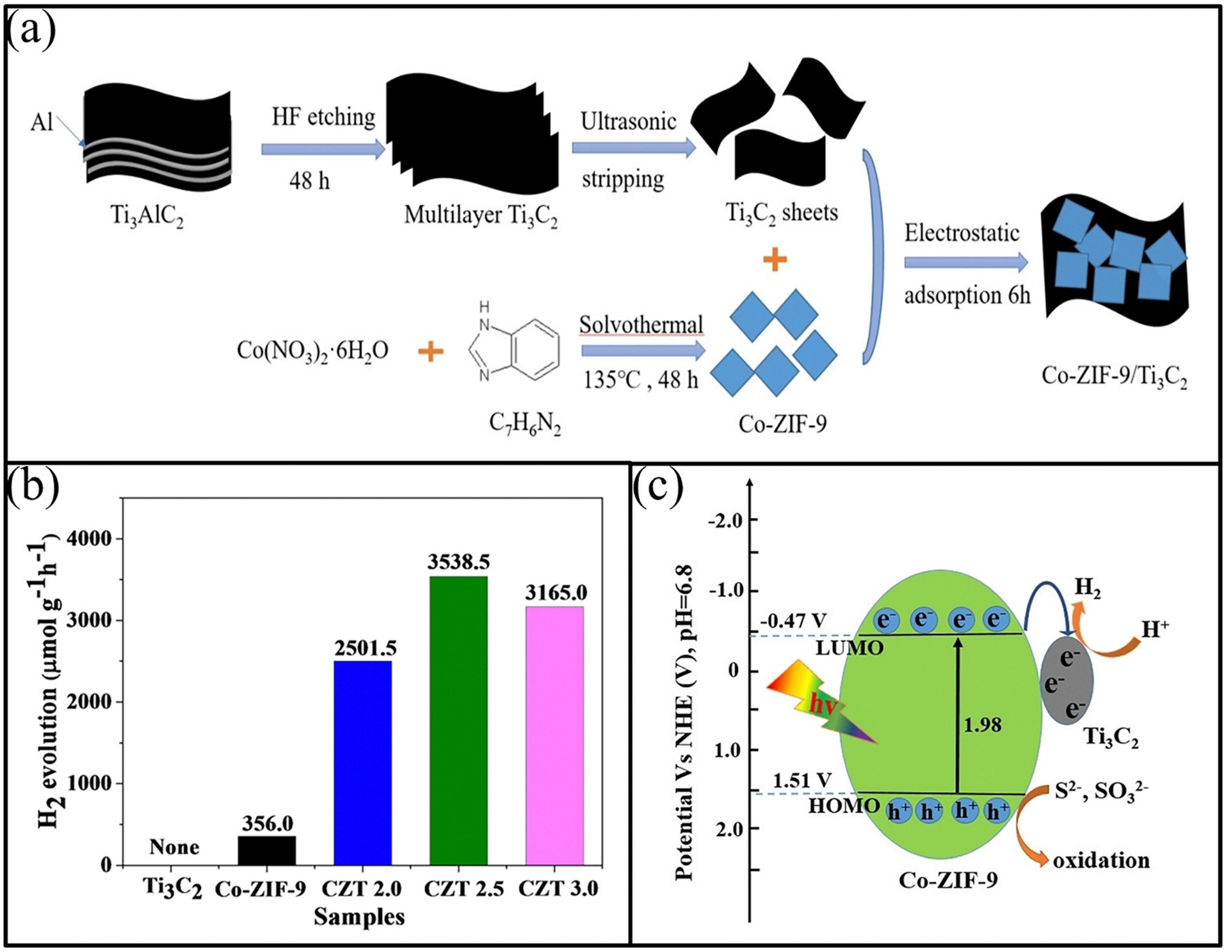

Fig. 14 (a) Synthesis of Co-ZIF-9/Ti_3C_2, (b) comparison of the H_2-production rate over different samples, and (c) mechanism for H_2-evolution over the Co-ZIF-9/Ti_3C_2. Reproduced with permission from ref. 105. Copyright 2022.

MOF/MXene hybrids and highlight the importance of rational interfacial engineering guided by theory. A summary of photocatalytic hydrogen production along with other parameters is presented in Table 3. Many researchers have studied hydrogen production using MXene/MOF composites. For example, Li *et al.*[104] synthesized a Ti_3C_2@MIL-NH_2 nanocomposite (Fig. 12(a)). The BET surface area of the prepared catalyst was 69.2 m^2 g^{-1}. The bandgap of the synthesized materials was 2.40 eV. The prepared nanocomposite was utilized as a catalyst for hydrogen production. The Ti_3C_2@MIL-NH_2 showed hydrogen evolution activity of 4383.1 μmol h^{-1} g^{-1} (Fig. 12(b)), with an apparent quantum yield of 3.140%, which was 6 times higher, and 5 times higher than that shown by pristine MIL-NH_2 and the physical mixture of MIL-NH_2 and Ti_3C_2. The Ti_3C_2@MIL-NH_2 showed higher efficiency due to the presence of Ti_3C_2. This is due to the fact that Ti_3C_2 enhances the charge carrier mobility and separation, thereby reducing the charge carrier recombination rate. The proposed mechanisms are given in Fig. 12(c).

Rajan *et al.*[101] prepared a Ni-MOF/CN/TC catalyst for hydrogen production. The bandgap of the synthesized catalyst was 2.1 eV. The Ni-MOF/CN/TC catalyst produces 1044.46 μmol g^{-1} hydrogen at pH 11 in the presence of solar light (1.5AM$_0$) using TEOA as a sacrificial agent. Ti_3C_2 (TC) was used as a co-catalyst. The TC has different weight%, namely 4, 8, and 12, which were labeled as 15Ni-MOF/CN/4TC, 15Ni-MOF/CN/8TC and 15Ni-MOF/CN/12TC, respectively. The hydrogen generation was determined to be 800.54 μmol g^{-1}, 1044.46 μmol g^{-1} and 910.25 μmol g^{-1}, for 15Ni-MOF/CN/4TC, 15Ni-MOF/CN/8TC and 15Ni-MOF/CN/12TC, respectively. However, despite having high concentration of TC, the 15Ni-MOF/CN/12TC showed lower hydrogen production rate because a higher concentration of TC occupied the active sites of 15Ni-MOF and also shielded the incident light. The sacrificial agent in the production of hydrogen was TEOA. Similarly, Shi *et al.* (2022) synthesized a UZT/CFMX nanocomposite as a photocatalyst for hydrogen production (Fig. 13(a)). The surface area of the prepared composite was calculated to be 371.9 m^2 g^{-1}. The bandgap of the prepared nanocomposite was 2.82 eV (Fig. 13(b)). The UZT/CFMX showed the hydrogen production rate of 2187 μmol g^{-1} h^{-1}, which was 20 times greater than that of pristine UZT and four times higher than that of UZT/MX (Fig. 13(c)). The

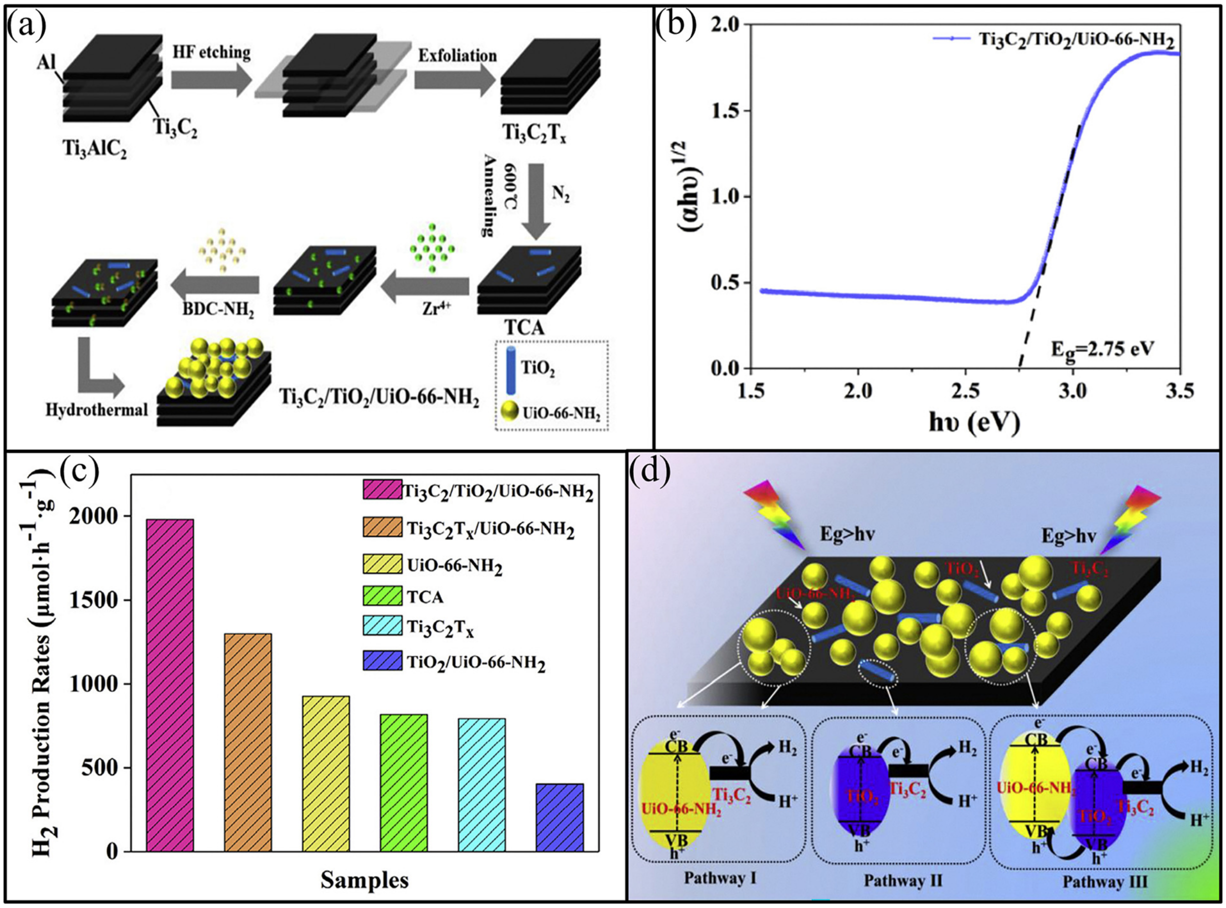

Fig. 15 (a) Diagrammatic representation of a possible chemical route for the synthesis of Ti_3C_2/TiO_2/UiO-66-NH_2, (b) bandgap for the Ti_3C_2/TiO_2/UiO-66 NH_2 nanocomposite, (c) the as-prepared samples had average H_2 production, and (d) the charge-transfer paths for Ti_3C_2/TiO_2/UiO-66-NH_2 are shown schematically. Reproduced with permission from ref. 52. Copyright 2019, Elsevier.

mechanisms of UZT/CFMX for hydrogen production are provided in Fig. 13(d).

Sun *et al.*[105] prepared a Co-ZIF-9/Ti_3C_2 nanocomposite as a photocatalyst for hydrogen production (Fig. 14(a)). 53.0 m^2 g^{-1} was the surface area of the synthesized photocatalyst. The Co-ZIF-9/Ti_3C_2 had a hydrogen production rate of 3538.5 μmol g^{-1} h^{-1}. The Co-ZIF-9/Ti_3C_2 was synthesized with various weight% of Ti_3C_2, *i.e.*, 2.0 wt%, 2.5 wt%, and 3.0 wt%, which were denoted as CZT2.0, CZT2.5 and CZT3.0, respectively. CZT2.5 had the highest hydrogen production, which was 3538.5 μmol g^{-1} h^{-1}, which was 9.6 times as high as that of pristine Co-ZIF-9. The Co-ZIF-9 had a low photocatalytic activity of 356.0 μmol g^{-1} h^{-1}, because of the quick recombination of e^- and h^+. The hydrogen production rate of the different catalysts is given in Fig. 14(b). The apparent quantum yield of the prepared photocatalysts was 4.8% at 420 nm. The sacrificial agent was Na_2S (0.1 M)/Na_2SO_3 (0.5 M). A 300 W xenon lamp was the light source. The mechanism for H_2-production over the Co ZIF-9/Ti_3C_2 composite is given in Fig. 14(c).

Tian *et al.*[52] synthesized a Ti_3C_2/TiO_2/UiO-66-NH_2 nanocomposite as a photocatalyst for hydrogen production (Fig. 15(a)). The prepared photocatalyst had a surface area and bandgap of 987.5 m^2 g^{-1} and 2.75 eV, respectively (Fig. 15(b)). The prepared photocatalysts were utilized for hydrogen generation. Ti_3C_2/TiO_2/UiO-66-NH_2 had a hydrogen evolution activity of 1980 μmol h^{-1} g^{-1}, which was about 2.5 times and 1.5 times higher than that of UiO-66-NH_2 and $Ti_3C_2T_x$/UiO-66-NH_2, respectively. The hydrogen production rate of the different materials is given in Fig. 15(c). The hydrogen production rate increases by the addition of TCA (co-catalysts). The proposed mechanisms for hydrogen production are given in Fig. 15(d).

3.2.1 Mechanisms of hydrogen production by MOF/MXene composites. The photocatalytic water splitting process can be divided into two main stages: PEC (photo-electrochemical) and photocatalytic reactions.[110] In particular, the PEC process utilizes light energy to initiate a chemical reaction that results in hydrogen (H_2) production. During this process, a semiconductor material is typically submerged in an electrolyte solution to enable the reaction. Upon exposure to light, the semiconductor absorbs photons, initiating the generation of e^-, h^+ pairs. These excited charge carriers are then separated by an internal electric field or an externally applied

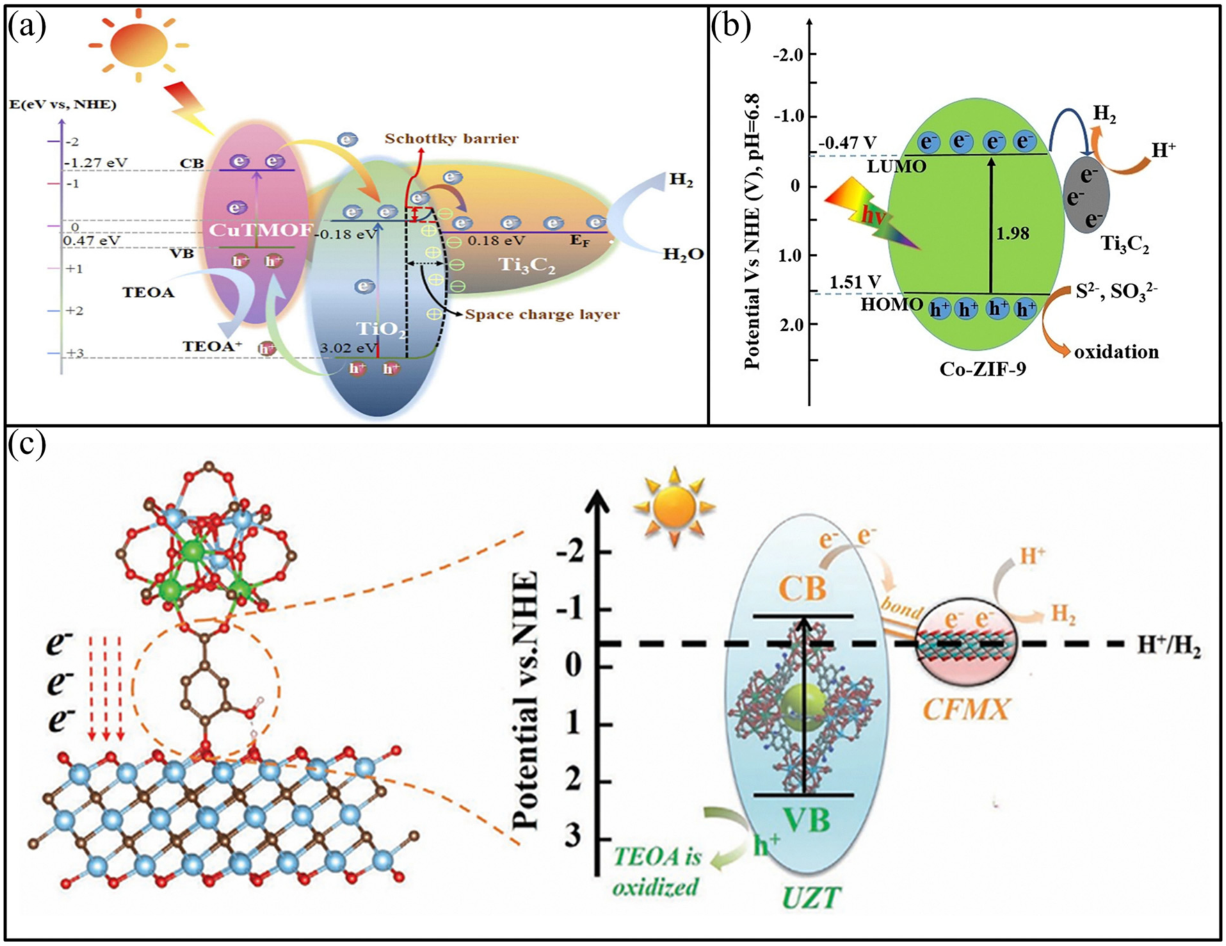

Fig. 16 (a) TT/CuTMOF nanocomposite photocatalytic mechanism. Reproduced with permission from ref. 107. Copyright 2023, Elsevier. (b) Possible photocatalytic mechanism for H_2-evolution over the Co ZIF-9/Ti_3C_2 composite. Reproduced with permission from ref. 105. Copyright 2022. (c) Schematic of the photocatalytic water splitting mechanism for UZT/CFMX. Reproduced with permission from ref. 101. Copyright 2022 open access CC BY 4.0.

bias, a phenomenon known as charge separation. Next, in a redox mechanism, the excited electrons migrate to the cathode (also known as the photocathode) whereas they reduce water molecules to form hydrogen gas. Simultaneously, the photo-generated h^+ move to the photoanode, where they oxidize water to generate oxygen. These electrons flow through an external circuit from the photoanode to the photocathode, completing the circuit in a process called electron transfer. This led to the final stage known as gas evolution, where hydrogen is released at the cathode and oxygen at the anode. When light with energy exceeding the semiconductor band gap strikes the photoanode, electrons are excited into the CB, while h^+ remain in the VB. These photogenerated electrons travel through the external circuit to reach the cathode, facilitated by the potential difference across the photoanode. At the cathode, protons (H^+) in the solution are reduced to form hydrogen gas.[111] A possible mechanism for photocatalytic hydrogen production is illustrated in Fig. 16. In this mechanism, light energy excites the semiconductor (SC) producing an e^-, h^+ pair (eqn (9)). The hole participates in oxidizing water molecules, producing protons and releasing oxygen gas (eqn (10)). This oxidation reaction is a crucial part of the overall water splitting process, which releases electrons, protons, and oxygen (eqn (11)). Finally, the generated electrons reduce protons to produce molecular hydrogen (eqn (12)). Overall, the water splitting reaction yields hydrogen and oxygen gases, requiring an energy input of 237 kJ mol^{-1} (overall reaction) (reaction (13)).[94]

$$\text{Light absorption: sc} + h\nu \rightarrow e^- + h^+ \tag{9}$$

$$\text{Oxidation of water: } 4h^+ + 2H_2O \rightarrow 4H^+ + O_2 \tag{10}$$

$$\text{Water splitting reaction: } 2H_2O \rightarrow O_2 + 4H^+ + 4e^- \tag{11}$$

$$\text{Reduction of protons: } 4H^+ + 4e^- \rightarrow 2H_2 \tag{12}$$

$$\text{Overall water splitting: } 2H_2O \rightarrow 2H_2 + O_2 \quad \Delta G = 237\ \text{kJ mol}^{-1} \tag{13}$$

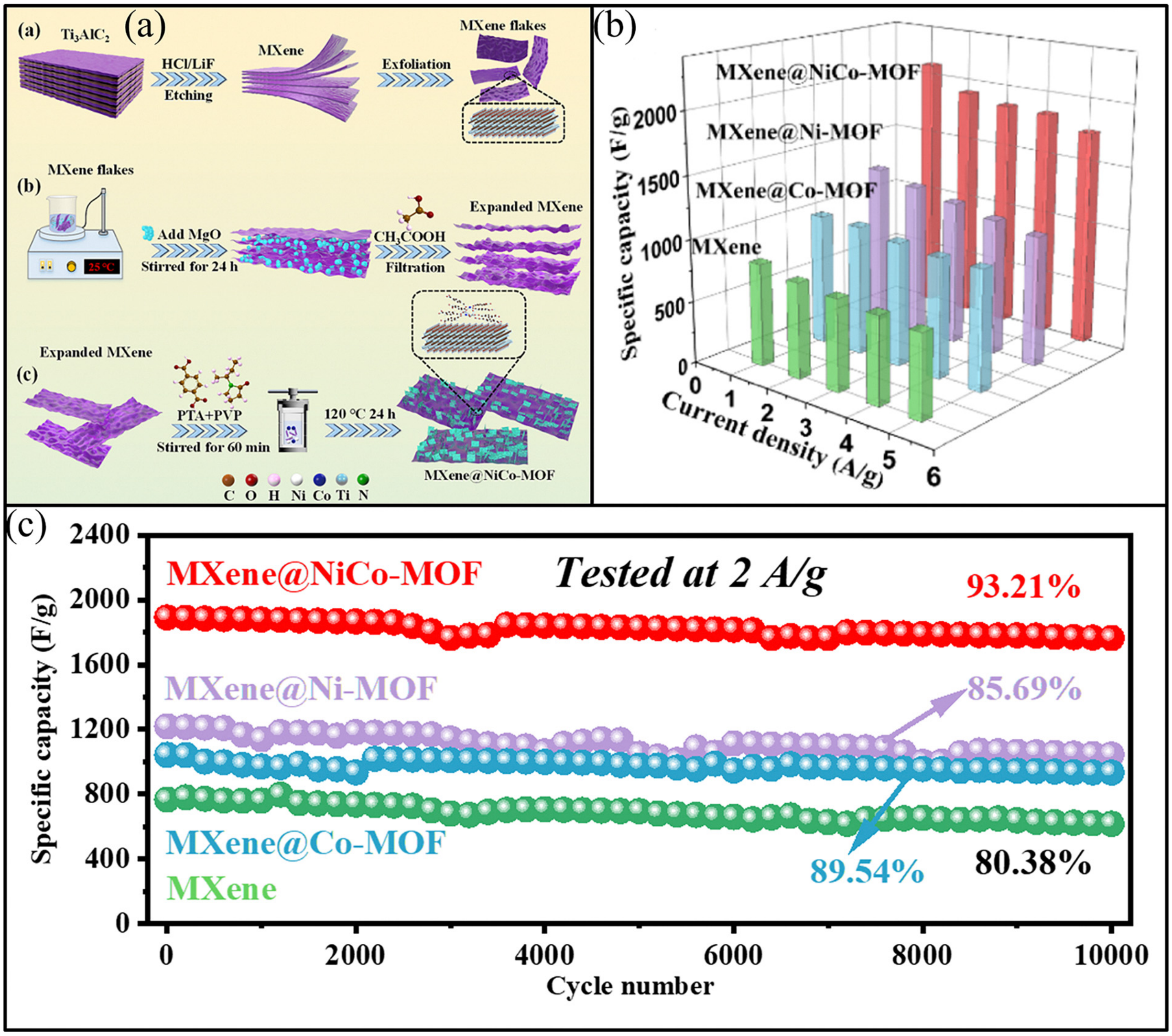

Fig. 17 (a) A simplified representation of the fabrication method of the MXene@NiCo-MOF, (b) specific capacitance of four electrodes, and (c) cycling stability for 10 000 cycles of the as-prepared electrode. Reproduced with permission from ref. 114. Copyright 2024, Elsevier.

3.3 Energy storage as a supercapacitor by the MOF/MXene composites

Supercapacitors, also known as ultracapacitors or electrochemical capacitors, are energy storage devices that bridge the gap between traditional capacitors and batteries. They store energy through electrostatic double-layer capacitance, enabling high power density and rapid charging/discharging capabilities.[112] With their ability to deliver high power pulses, supercapacitors are suitable for applications requiring rapid energy storage and release. They also boost the long cycle life, withstanding millions of charge/discharge cycles, and can charge discharge quickly.[113] These properties make supercapacitors ideal for various applications, including energy storage. By storing energy generated from renewable sources and releasing it when needed, supercapacitors can help improve energy efficiency and reduce our reliance on fossil fuels.[26] For example, Wei *et al.* (2024) prepared a MXene@NiCo-MOF nanocomposite and used it as an anode (Fig. 17(a)). The prepared nanomaterial surface area was 50.63 $m^2\ g^{-1}$. The synthesized nanocomposite had the energy density and power density of 40.23 Wh kg^{-1} and 1495.07 W kg^{-1}, respectively. The capacitance of the prepared nanocomposite was 2720 (F g^{-1}) at a current density of 1 A g^{-1}, respectively (Fig. 17(b)). The capacitance retention was found to be 93.21% after 10 000 cycles (Fig. 17(c)). The electrolyte used in MXene@NiCo-MOF was 2 M KOH.[114] Table 4 depicts the MXene/MOF-based supercapacitors.

Thakur *et al.*[26] synthesized a $Ti_3C_2T_x$/Ni-MOF nanocomposite through a solvothermal method for use as an electrode material for supercapacitors (Fig. 18(a)). The surface area of the synthesized nanomaterial was 166 $m^2\ g^{-1}$. The power density and energy density of the prepared nanomaterial were 331.8 W kg^{-1} and 19.4 Wh kg^{-1}, respectively. The capacitance of the synthesized nanocomposite was 139.4 F g^{-1} at a current density of 1 A g^{-1}, respectively (Fig. 18(b)). Capacitance retention was determined to be 95% after 5000 cycles (Fig. 18(c)). Polyvinyl alcohol in 1 M H_2SO_4 was used as an electrolyte.

Table 4 Summary of MOF/MXene composites for supercapacitors

MOF/MXene composite	Electrolyte	Surface area ($m^2\ g^{-1}$)	Capacitance	Current density/scan rate ($A\ g^{-1}$)	Energy density ($Wh\ kg^{-1}$)	Power density ($kW\ kg^{-1}$)	Capacitance retention (cycles)	Ref.
CA@MIL-101-(Cr)/Ti_3C_2T	KOH	208	2720 ($F\ g^{-1}$)	1.5	38	1280	84%/10 000	115
MXene@NiCo-MOF	2 M KOH	50.63	2078.1 $F\ g^{-1}$	2	40.23	1495.07	93.21%/10 000	114
MIL-100(Fe)/Ti_3C_2	KOH	529.49	962.17 $F\ g^{-1}$	0.5	85.53	200	93%/10 000	116
MOF/MXene/NF-300//AC/NF	1 M KOH		2453 $F\ g^{-1}$	1	46.3	746.8	118.1%/15 000	117
NiCo-MOF/$Ti_3C_2T_x$	2 M KOH	22.56	815.2 $A\ g^{-1}$	1	39.5	562.5	82.3%/10 000	118
MOF-5/V_2CT_x//AC	3 M KOH	83	235 $C\ g^{-1}$	2–3.5	48.75	920	95%/16 000	119
M-NC@NCM/NF	NiCo solution		2137.5 $F\ g^{-1}$	1	32.6	7000	75.3%/5000	120
$Ti_3C_2T_x$/Ni-MOFs	6 M KOH	96.6	1124 $F\ g^{-1}$	1	46	0.8	74.8%/4000	121
CoTC-300//AC	1.0 M KOH		217.3 $C\ cm^{-3}$)	10 $A\ m^{-2}$	176.3	337.5 $W\ L^{-1}$	100%/5000	122
Ni/Co-MOF@TCT-NH_2//AC	3.0 M KOH	129.22	1924 $F\ g^{-1}$	0.5	98.1	600	99.3%/15 600	123
Ni-MOF/MXene	1 M KOH		716.19 $F\ g^{-1}$	1	23.28	2.841	97.84%/2000	27
100 MX-MN	2 M KOH	251. 77	1028 $C\ g^{-1}$	1	87. 35	1.98	88%/10 000	56
$Ti_3C_2T_x$/Ni-MOF	Polyvinyl alcohol in 1 M H_2SO_4	166	139.4 $F\ g^{-1}$	1	19.4	331.8	95%/5000	26
Ni-MOF/$Ti_3C_2T_x$	KOH/PVA	167.74	497.6 $F\ g^{-1}$	0.5	223.9	1953.3	85%/1000	124
MnO_2@Co_3O_4-PC@MX-CNF	PVA/KOH		475.4 $mAh\ g^{-1}$	1	72.5	832.4	90.36%/10 000	125
NiCo-LDH/$Ti_3C_2T_x$-5	2 M KOH	121.38	635.7 $C\ g^{-1}$	1	44.6	852.5	85.71%/10 000	126
NiCo-MOF/$Ti_3C_2T_x$	2 M KOH	22.56	815.2 $F\ g^{-1}$	1	39.5	562.5	82.3%/10 000	118
M-$NiCo_2O_4$@NiCo-MOF/CC	3 M KOH		2091.0 $F\ g^{-1}$	1	56.7	750	90.3%/6000	127
MXene-FeCu MOF@NF	PVA/KOH		460 $mA\ h\ cm^{-2}$	3 $mA\ cm^{-2}$	33.3	503	89%/10 000	128

Shivade *et al.*[27] used a solvothermal approach to synthesize a Ni-MOF/MXene composite as a positive electrode for supercapacitors. They employed folic acid as a biological organic linker, in the preparation of the Ni-MOF/MXene composite. The power density and energy density of the prepared nanocomposite were 2.841 kW kg^{-1} and 23.28 Wh kg^{-1}, respectively. The synthesized Ni-MOF/MXene composite has a current density of 1 A g^{-1}, in a 1 M KOH electrolyte and current density capacitance of 716.19 F g^{-1}, respectively. The capacitance retention was found to be 97.84% after 2000 cycles. Shalini *et al.*[56] prepared 100 MX-MN nanocomposites as a positive electrode using the hydrothermal method (Fig. 19(a)). They prepared various ratios of MX, such as 50 mg, 75 mg, 100 mg, and 150 mg, termed 50 MX-MN, 75 MX-MN, 100 MX-MN, and 150 MX-MN, respectively (Fig. 19(b)). The BET surface area of 100 MX-MN was 251.77 $m^2\ g^{-1}$ (Fig. 19(c)). When compared to other materials, the materials with the highest surface area showed the best electrochemical properties. Electrochemical procedures such as GCD and CV were carried out. The specific capacity of the 100 MX-MN composite was 1028 C g^{-1} at a current density of 1 A g^{-1}, respectively. The specific capacity of all composites at 1 A g^{-1} is given in Fig. 19(d). The energy density of 100 MX-MN was 87. 35 Wh kg^{-1} and the power density was 1.98 kW kg^{-1}, respectively. After 10 000 cycles, 88% was the capacity retention.

4. Conclusion and future perspectives

MOF/MXene composites represent a highly promising class of multifunctional materials that synergistically integrate the high porosity, tunable framework, and catalytic versatility of MOFs with the superior electrical conductivity, mechanical strength, and surface functionality of MXenes. This overview provides a comprehensive summary of the synthesis strategies, structural architectures, and practical applications of these hybrids across diverse fields, including energy storage, catalysis, sensing, and environmental remediation. Despite the remarkable progress achieved, several challenges remain that directly influence their large-scale applicability and functional efficiency. The intrinsic instability and limited conductivity of conventional MOFs, combined with the oxidation sensitivity and surface degradation of MXenes, often lead to inconsistent interfacial bonding and compromised electronic pathways. Furthermore, the structural compatibility between the MOF frameworks and MXene layers significantly affects ion transport, active site accessibility, and overall charge-transfer efficiency, highlighting the importance of precise interface engineering. Similarly, the selection of metal nodes, organic linkers, and surface terminations plays a decisive role in tuning redox activity and catalytic selectivity. Understanding and optimizing these interfacial and compositional parameters are therefore central to improving performance consistency and device reliability. With rational structural design, advanced synthesis control, and deeper insight into interfacial phenomena,

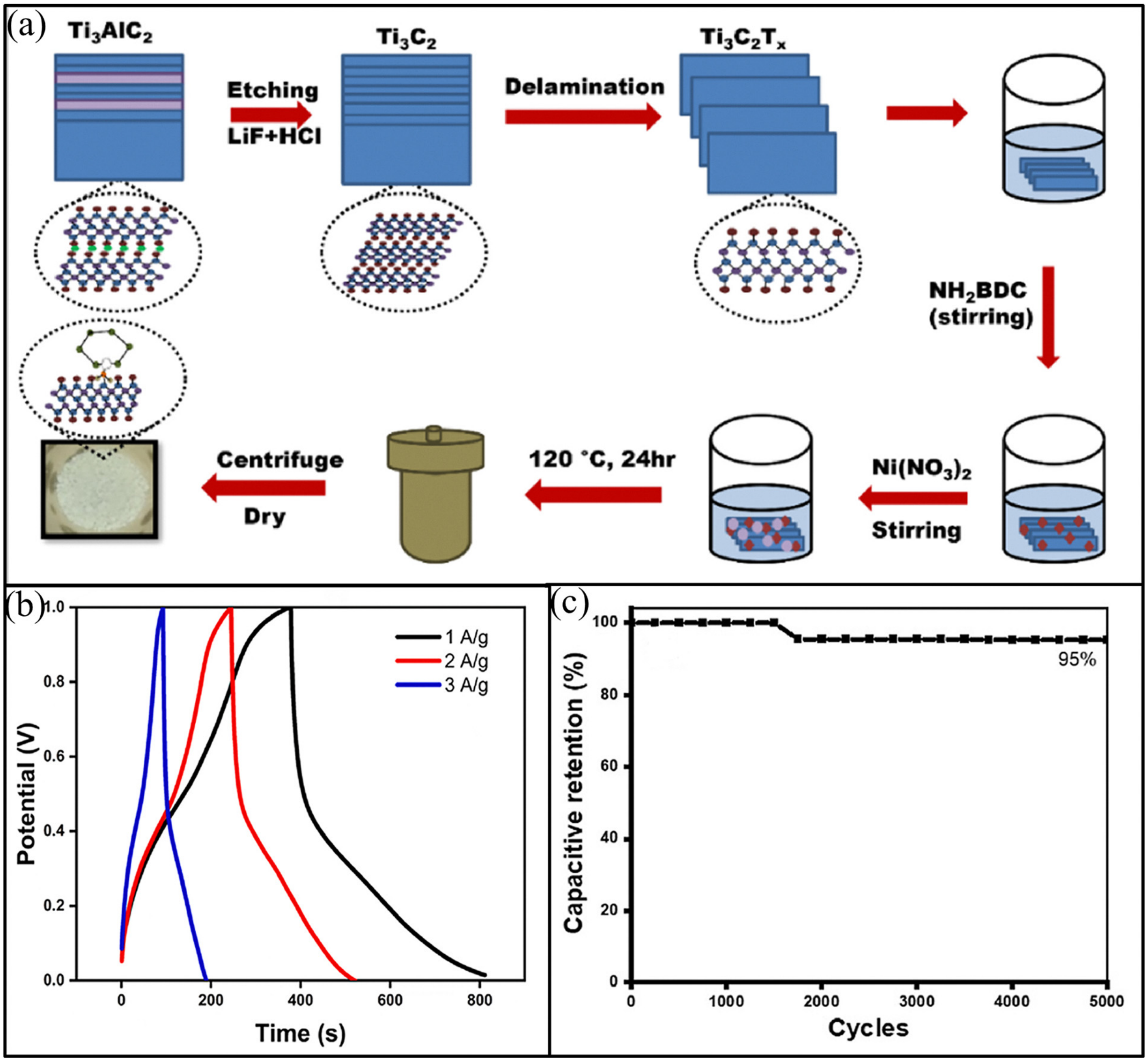

Fig. 18 (a) Schematic representation of the synthesis of the $Ti_3C_2T_x$/Ni-MOF composite, (b) GCD curve of the $Ti_3C_2T_x$/Ni-MOF composite at varied current densities, and (c) cycling stability performance of the device. Reproduced with permission from ref. 26. Copyright 2024, Elsevier.

MOF/MXene composites can evolve from promising laboratory materials to practical systems capable of addressing critical challenges in clean energy, environmental sustainability, and advanced sensing technologies.

Future research should prioritize the following essential directions:

4.1 Advance materials design

Look beyond traditional ZIF and MIL MOFs to discover new 2D/2D designs and heterostructures that improve charge transfer and increase electrochemical activity.

4.2 Interface engineering

Create strategies for controlled chemical and physical bonding between MOFs and MXenes, using surface functional groups to create well-ordered heterojunctions.

4.3 Green synthesis approaches

Shift to environmentally friendly and scalable fabrication techniques to enable industrial-scale manufacturing, abandoning harmful etchants and high-energy procedures.

4.4 *In situ* characterization and simulation

Use modern *in situ* instruments and computer simulations to better understand composite structural evolution, electronic interactions, and real time behavior under operational settings.

4.5 Application-specific optimization

Modulate factors such as morphology, dimensionality, and surface chemistry to optimize composite structures for improved performance in specific domains such as supercapacitors, photocatalysts and sensors.

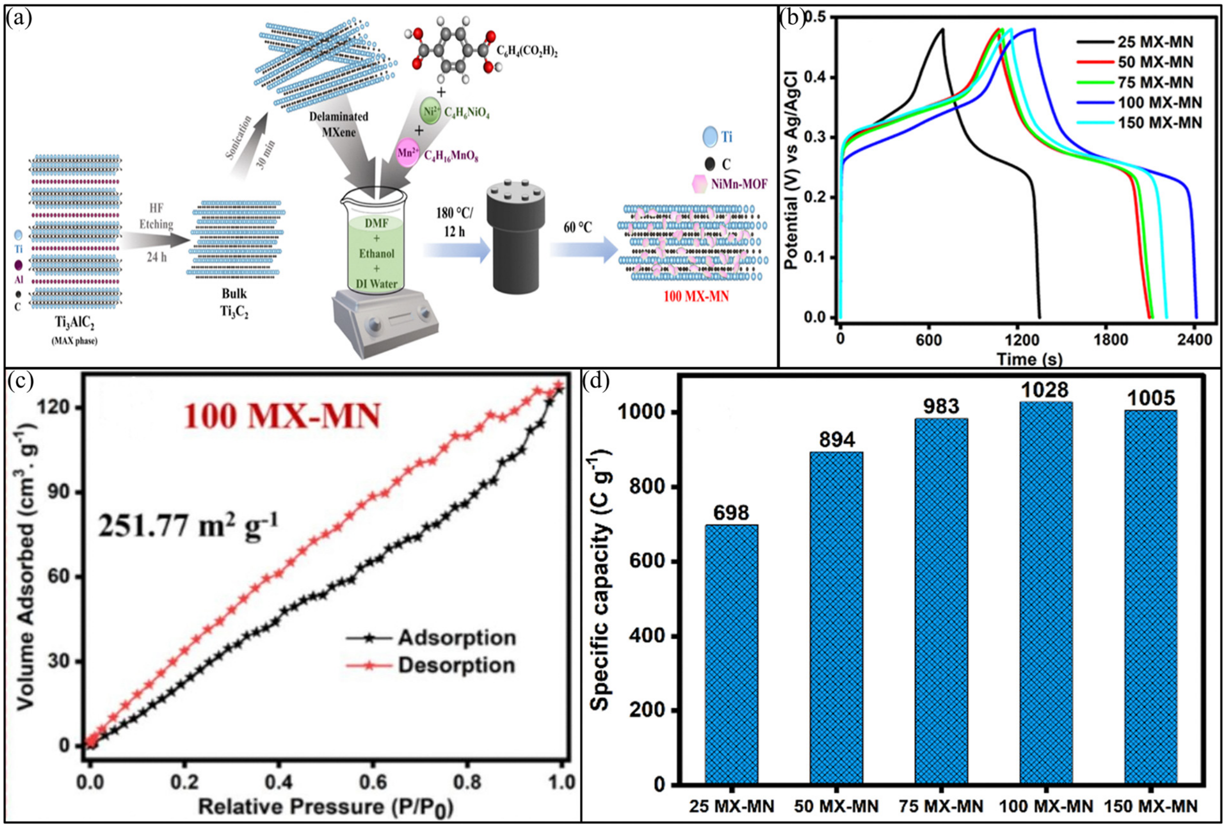

Fig. 19 (a) The schematic representation of etching aluminum from the MAX phase and the synthesis of composites. (b) The GCD curve at 1 A g^{-1}, (c) the nitrogen adsorption–desorption and pore distribution curves of the 100 MX-MN composite, and (d) specific capacity of all the composites at 1 A g^{-1}. Reproduced with permission from ref. 56. Copyright 2024, Elsevier.

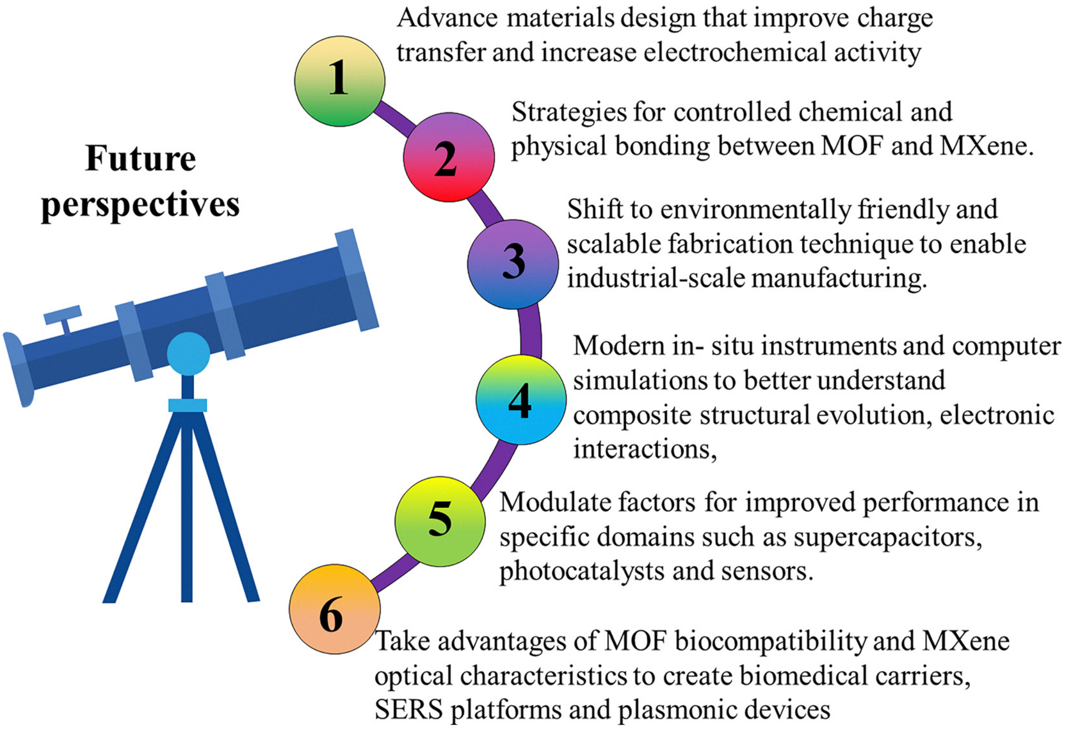

1 Advance materials design that improve charge transfer and increase electrochemical activity

2 Strategies for controlled chemical and physical bonding between MOF and MXene.

3 Shift to environmentally friendly and scalable fabrication technique to enable industrial-scale manufacturing.

4 Modern in- situ instruments and computer simulations to better understand composite structural evolution, electronic interactions,

5 Modulate factors for improved performance in specific domains such as supercapacitors, photocatalysts and sensors.

6 Take advantages of MOF biocompatibility and MXene optical characteristics to create biomedical carriers, SERS platforms and plasmonic devices

Fig. 20 Proposed future research direction for MXene/MOF composites.

4.6 Biological and photonic integration

Take advantage of MOF biocompatibility and MXene optical characteristics to create biomedical carriers, SERS platforms and plasmonic devices (Fig. 20).

Author contributions

Muhammad Kashif: conceptualization, data curation, investigation, methodology, visualization, writing – original draft. Syed Izaz Ali Shah: conceptualization, validation, writing – original draft. Salman Khan: conceptualization, visualization, writing – original draft. Sheraz Ahmad: resources, writing – review & editing. Muhammad Anwar and Sami Ur Rahman: resources, writing – review & editing. Shohreh Azizi: writing – review & editing. Malik Maaza: writing – review & editing.

Conflicts of interest

The authors declare no conflict of interest.

Data availability

Data sharing is not applicable to this review article, as no new data were generated or analysed in this study.

Acknowledgements

This research received funding from South African Coal, Oil, and Gas Corporation-National Research Foundation (SASOL-NRF) University Collaborative Research Grants (grant no. 138626) & (RA231026158193). The authors thank the SASOL National Research Foundation of South Africa (SASOL NRF) grant RC code 868400 and grant no: 138626.

References

1 S. khan, U. Kalsoom, M. Kashif, S. A. Hussain, M. Gul, S. Azizi and M. Maaza, *Water, Air, Soil Pollut.*, 2025, **236**, 900.

2 C. Medjili, N. Lakhdari, D. Lakhdari, A. Berchi, N. Osmani, I. Laourari, Y. Vasseghian and M. Berkani, *Chemosphere*, 2023, **313**, 137427.

3 C. Chinnasamy, N. Perumal, A. Choubey and S. Rajendran, *Environ. Res.*, 2023, 116459.

4 H. Bahramian, A. Fattah-alhosseini, M. Karbasi, E. Nikoomanzari and S. Giannakis, *Chem. Eng. J.*, 2023, **476**, 146588.

5 R. Hosseini, A. Fattah-alhosseini and M. Karbasi, *Surf. Interfaces*, 2023, **42**, 103311.

6 A. K. Pandey, D. V. Sarada and A. Kumar, *Proc. Natl. Acad. Sci., India, Sect. B*, 2016, **86**, 805–815.

7 A. Baban, A. Yediler, D. Lienert, N. Kemerdere and A. Kettrup, *Dyes Pigm.*, 2003, **58**, 93–98.

8 P. M. Ondarza, S. P. Haddad, E. Avigliano, K. S. Miglioranza and B. W. Brooks, *Sci. Total Environ.*, 2019, **649**, 1029–1037.

9 H. B. Quesada, A. T. A. Baptista, L. F. Cusioli, D. Seibert, C. de Oliveira Bezerra and R. Bergamasco, *Chemosphere*, 2019, **222**, 766–780.

10 M. Zilker, F. Sörgel and U. Holzgrabe, *J. Pharm. Biomed. Anal.*, 2019, **166**, 222–235.

11 S. Mahapatra, M. H. Ali and K. Samal, *Energy Nexus*, 2022, **6**, 100062.

12 L. A. Schaider, R. A. Rudel, J. M. Ackerman, S. C. Dunagan and J. G. Brody, *Sci. Total Environ.*, 2014, **468**, 384–393.

13 S. Webb, T. Ternes, M. Gibert and K. Olejniczak, *Toxicol. Lett.*, 2003, **142**, 157–167.

14 A. Aschengrau, J. M. Weinberg, P. A. Janulewicz, M. E. Romano, L. G. Gallagher, M. R. Winter, B. R. Martin, V. M. Vieira, T. F. Webster and R. F. White, *Environ. Health*, 2011, **10**, 1–13.

15 N. Z. Arman, S. Salmiati, A. Aris, M. R. Salim, T. H. Nazifa, M. S. Muhamad and M. Marpongahtun, *Water*, 2021, **13**, 3258.

16 C. Zwiener, *Anal. Bioanal. Chem.*, 2007, **387**, 1159–1162.

17 F. Dawood, M. Anda and G. Shafiullah, *Int. J. Hydrogen Energy*, 2020, **45**, 3847–3869.

18 R. Rincón, A. Marinas, J. Muñoz, C. Melero and M. Calzada, *Chem. Eng. J.*, 2016, **284**, 1117–1126.

19 J. D. Holladay, J. Hu, D. L. King and Y. Wang, *Catal. Today*, 2009, **139**, 244–260.

20 M. Tahir, *Energy Fuels*, 2024.

21 S. C. Hui, *Comput. Methods Programs Biomed.*, 2007, **88**(3), 283–294.

22 C.-J. Winter, *Int. J. Hydrogen Energy*, 2005, **30**, 681–685.

23 F. Zhang, P. Zhao, M. Niu and J. Maddy, *Int. J. Hydrogen Energy*, 2016, **41**, 14535–14552.

24 N. Serpone, D. Lawless and R. Terzian, *Sol. Energy*, 1992, **49**, 221–234.

25 T. Ramachandran, F. Hamed, R. K. Raji, S. M. Majhi, D. Barik, Y. A. Kumar, R. M. Jauhar, M. Pachamuthu, L. Vijayalakshmi and S. Ansar, *J. Phys. Chem. Solids*, 2023, **180**, 111467.

26 K. K. Thakur, A. L. Sharma and S. Singh, *Mater. Chem. Phys.*, 2024, **322**, 129463.

27 D. S. Shivade, A. N. Kurade, R. K. Bhosale, S. S. Kundale, A. R. Shelake, A. D. Patil, P. P. Waifalkar, R. K. Kamat, A. M. Teli and T. D. Dongale, *J. Energy Storage*, 2024, **100**, 113754.

28 J. Xie, C. Yang, M. Duan, J. Tang, Y. Wang, H. Wang and J. Courtois, *Ceram. Int.*, 2018, **44**, 5459–5465.

29 M. Liu, L. Zhou, X. Luo, C. Wan and L. Xu, *Catalysts*, 2020, **10**, 788.

30 A. N. Hong, H. Yang, X. Bu and P. Feng, *EnergyChem*, 2022, **4**, 100080.

31 W. Peng, L. Han, Y. Gao, Z. Gong, T. Lu, X. Xu, M. Xu, Y. Yamauchi and L. Pan, *J. Colloid Interface Sci.*, 2022, **608**, 396–404.

32 X. Liu, Y. Shan, S. Zhang, Q. Kong and H. Pang, *Green Energy Environ.*, 2023, **8**, 698–721.

33 S. Lin, Z. Song, G. Che, A. Ren, P. Li, C. Liu and J. Zhang, *Microporous Mesoporous Mater.*, 2014, **193**, 27–34.

34 T. Qin, Z. Wang, Y. Wang, F. Besenbacher, M. Otyepka and M. Dong, *Nano-Micro Lett.*, 2021, **13**, 183.

35 S. K. Sharma, A. Kumar, G. Sharma, D.-V. N. Vo, A. García-Peñas, O. Moradi and M. Sillanpää, *Chemosphere*, 2022, **291**, 132923.

36 Y. Lee, S. J. Kim, Y.-J. Kim, Y. Lim, Y. Chae, B.-J. Lee, Y.-T. Kim, H. Han, Y. Gogotsi and C. W. Ahn, *J. Mater. Chem. A*, 2020, **8**, 573–581.

37 Z. Hao, S. Zhang, S. Yang, X. Li, Y. Gao, J. Peng, L. Li, L. Bao and X. Li, *ACS Appl. Energy Mater.*, 2022, **5**, 2898–2908.

38 X. Yang, Y. Yao, Q. Wang, K. Zhu, K. Ye, G. Wang, D. Cao and J. Yan, *Adv. Funct. Mater.*, 2022, **32**, 2109479.

39 X. Zhang, X. Liu, Y. Feng, S. Qiu, Y. Shao, Q. Liao, H. Li and Y. Liu, *Appl. Mater. Today*, 2022, **27**, 101483.

40 W. Qian, Y. Si, P. Chen, C. Tian, Z. Wang, P. Li, S. Li and D. He, *Small*, 2024, **20**, 2403149.

41 U. Kalsoom, S. Khan, M. Kashif, H. S. Yaseen, S. A. Hussain, S. Azizi and M. Maaza, *Ionics*, 2025, DOI: **10.1007/s11581-025-06628-z**.

42 S. Venkateswarlu, S. Vallem, M. Umer, N. Jyothi, A. G. Babu, S. Govindaraju, Y. Son, M. J. Kim and M. Yoon, *J. Energy Chem.*, 2023, **86**, 409–436.

43 X. Zhuang, S. Zhang, Y. Tang, F. Yu, Z. Li and H. Pang, *Coord. Chem. Rev.*, 2023, **490**, 215208.

44 G. Yang and S.-J. Park, *Materials*, 2019, **12**, 1177.

45 T. Ramachandran, A. H. I. Mourad, R. K. Raji, R. Krishnapriya, N. Cherupurakal, A. Subhan and Y. Al-Douri, *Int. J. Energy Res.*, 2022, **46**, 16823–16838.

46 M. A. Nazir, M. S. Bashir, M. Jamshaid, A. Anum, T. Najam, K. Shahzad, M. Imran, S. S. A. Shah and A. ur Rehman, *Surf. Interfaces*, 2021, **25**, 101261.

47 Z. Hu, Y. Wang and D. Zhao, *Acc. Mater. Res.*, 2022, **3**, 1106–1114.

48 B. Liu, K. Vellingiri, S.-H. Jo, P. Kumar, Y. S. Ok and K.-H. Kim, *Nano Res.*, 2018, **11**, 4441–4467.

49 A. Nandagudi, S. Nagarajarao, M. Santosh, B. Basavaraja, S. Malode, R. Mascarenhas and N. Shetti, *Mater. Today Sustain*, 2022, **19**, 100214.

50 Y. Pan, J. Wang, X. Guo, X. Liu, X. Tang and H. Zhang, *J. Colloid Interface Sci.*, 2018, **513**, 418–426.

51 Y. Wu, X. Li, Q. Yang, D. Wang, F. Yao, J. Cao, Z. Chen, X. Huang, Y. Yang and X. Li, *Chem. Eng. J.*, 2020, **390**, 124519.

52 P. Tian, X. He, L. Zhao, W. Li, W. Fang, H. Chen, F. Zhang, Z. Huang and H. Wang, *Int. J. Hydrogen Energy*, 2019, **44**, 788–800.

53 X. Yu, Y. Hu, X. Luan, S. J. Shah, L. Liu, C. Li, Y. Ren, L. Zhou, J. Li and J. Deng, *Chem. Eng. J.*, 2023, **476**, 146878.

54 P. Tian, X. He, L. Zhao, W. Li, W. Fang, H. Chen, F. Zhang, Z. Huang and H. Wang, *Sol. Energy*, 2019, **188**, 750–759.

55 F. Yang, J. Li, J. Dong, S. Chen, W. Hu, Y. Zhang, H. Wang, Z. Li and Z. Wang, *Sep. Purif. Technol.*, 2024, **337**, 126488.

56 S. S. Shalini, Y.-P. Fu and A. C. Bose, *Chem. Eng. J.*, 2024, **500**, 156751.

57 N. Liu, Y. Zheng, C. Jing, B. Gao, W. Huang, Z. Li, J. Lei, X. Zhang, L. Cui and L. Tang, *J. Mol. Liq.*, 2020, **311**, 113201.

58 Z.-F. Lin, T.-H. Wang, P. Venkatesan and R.-A. Doong, *Chem. Eng. J.*, 2025, **505**, 159411.

59 S. Eslaminejad, R. Rahimi and M. Fayazi, *J. Ind. Eng. Chem.*, 2025, **141**, 94–103.

60 J. Gu, H. Fan, C. Li, J. Caro and H. Meng, *Angew. Chem.*, 2019, **131**, 5351–5355.

61 W. Xiang, Y. Zhang, H. Lin and C.-J. Liu, *Molecules*, 2017, **22**, 2103.

62 L. Cheng, Y. Tang, M. Xie, Y. Sun and H. Liu, *J. Alloys Compd.*, 2021, **864**, 158913.

63 S. Liu, X. Jiang, G. I. Waterhouse, Z.-M. Zhang and L.-M. Yu, *Sep. Purif. Technol.*, 2022, **294**, 121094.

64 K. Zhang, Y. Zhu, K. Yue, K. Zhan, P. Wang, Y. Kong, Y. Yan and X. Wang, *Nano Res.*, 2023, **16**, 3672–3679.

65 J. Zhu, W. Nie, Q. Wang, J. Li, H. Li, W. Wen, T. Bao, H. Xiong, X. Zhang and S. Wang, *Carbon*, 2018, **129**, 29–37.

66 Z.-Q. Li, L.-G. Qiu, T. Xu, Y. Wu, W. Wang, Z.-Y. Wu and X. Jiang, *Mater. Lett.*, 2009, **63**, 78–80.

67 H. He, X. Wang, Q. Yu, W. Wu, X. Feng, D. Kong, X. Ren and J. Gao, *Catalysts*, 2023, **13**, 876.

68 H. S. Far, M. Najafi, E. Moradi, M. Atighi, M. Rabbani and M. Hasanzadeh, *J. Mol. Struct.*, 2024, **1312**, 138627.

69 H. S. Far, M. Najafi, M. Hasanzadeh and R. Rahimi, *Inorg. Chem. Commun.*, 2023, **152**, 110680.

70 H. T. Pham, J. Y. Choi, X. Fang, A. Claman, S. Huang, S. Coates, L. Wayment, W. Zhang and J. Park, *Chem*, 2024, **10**, 199–210.

71 H. T. Pham, J. Y. Choi, M. Stodolka and J. Park, *Acc. Chem. Res.*, 2024, **57**, 580–589.

72 C. Huang, W. Sun, Y. Jin, Q. Guo, D. Mücke, X. Chu, Z. Liao, N. Chandrasekhar, X. Huang and Y. Lu, *Angew. Chem., Int. Ed.*, 2024, **63**, e202313591.

73 X. Xiao, X. Peng, H. Jin, T. Li, C. Zhang, B. Gao, B. Hu, K. Huo and J. Zhou, *Adv. Mater.*, 2013, **25**, 5091–5097.

74 D. Huang, L. Chen, L. Yue, F. Yang, H. Guo and W. Yang, *J. Alloys Compd.*, 2021, **867**, 158764.

75 G. Nagaraju, S. C. Sekhar, B. Ramulu and J. S. Yu, *Energy Storage Mater.*, 2021, **35**, 750–760.

76 J. Kim, C. Young, J. Lee, Y.-U. Heo, M.-S. Park, M. S. A. Hossain, Y. Yamauchi and J. H. Kim, *J. Mater. Chem. A*, 2017, **5**, 15065–15072.

77 L. Sun, Y. Chen, K. Zhuo, D. Sun, J. Liu and J. Wang, *Electrochim. Acta*, 2023, **466**, 143005.

78 I. Dědek, V. Kupka, P. Jakubec, V. Šedajová, K. Jayaramulu and M. Otyepka, *Appl. Mater. Today*, 2022, **26**, 101387.

79 N. K. Pavithra Siddu, S. M. Jeong and C. S. Rout, *Energy Adv.*, 2024, **3**, 341–365.

80 M. Ibrahim, M. G. Fayed, S. G. Mohamed, Z. Wen, X. Sun and H. N. Abdelhamid, *ACS Appl. Energy Mater.*, 2022, **5**, 12828–12836.

81 H. T. Pham, J. Y. Choi, S. Huang, X. Wang, A. Claman, M. Stodolka, S. Yazdi, S. Sharma, W. Zhang and J. Park, *J. Am. Chem. Soc.*, 2022, **144**, 10615–10621.

82 S. Zhou, T. Liu, M. Strømme and C. Xu, *Angew. Chem., Int. Ed.*, 2024, **63**, e202318387.

83 A. Fattah-alhosseini, Z. Sangarimotlagh, M. Karbasi and M. Kaseem, *Nano-Struct. Nano-Objects*, 2024, **38**, 101192.

84 R. R. Zairov, A. Syed, M. M. Tawfiq, A. F. Al-Hussainy, A. S. Mansoor, U. K. Radi, A. H. Idan, H. Bahair, H. A. Al-Shwaiman and M. Subramaniam, *Spectrochim. Acta, Part A*, 2025, **327**, 125406.

85 D. Wu, Z. Tong, J. Wang, G. Chen, A. Zhu, H. Tong and M. Dang, *Sep. Purif. Technol.*, 2025, **359**, 130873.

86 Q. Tan, Z. Yu, Q. Xiang, N. He, R. Long and J. Wang, *Process Saf. Environ. Prot.*, 2023, **179**, 405–420.

87 Y. Cao, L. Yue, Z. Li, Y. Han, J. Lian, H. Qin and S. He, *Appl. Surf. Sci.*, 2023, **609**, 155191.

88 Z. Li, S. Ning, F. Hu, H. Zhu, L. Zeng, L. Chen, X. Wang, T. Fujita and Y. Wei, *J. Colloid Interface Sci.*, 2023, **629**, 97–110.

89 B. Tan, Y. Fang, Q. Chen, X. Ao and Y. Cao, *J. Colloid Interface Sci.*, 2021, **601**, 581–593.

90 Z. Fan, X. Zhang, Y. Li, X. Guo and Z. Jin, *J. Ind. Eng. Chem.*, 2022, **110**, 491–502.

91 K. Yang, T. Liu, D. Xiang, Y. Li and Z. Jin, *Sep. Purif. Technol.*, 2022, **298**, 121564.

92 S. Rafiq, S. Awan, R.-K. Zheng, Z. Wen, M. Rani, D. Akinwande and S. Rizwan, *J. Magn. Magn. Mater.*, 2020, **497**, 165954.

93 V. Q. Hieu, T. K. Phung, T.-Q. Nguyen, A. Khan, V. D. Doan, V. A. Tran and V. T. Le, *Chemosphere*, 2021, **276**, 130154.

94 S. I. A. Shah, W. Ahmad, M. Anwar, R. Shah, J. A. Khan, N. S. Shah, A. Al-Anazi and C. Han, *Appl. Catal. O: Open*, 2025, 207049.

95 I. Vamvasakis, A. Trapali, J. Miao, B. Liu and G. S. Armatas, *Inorg. Chem. Front.*, 2017, **4**, 433–441.

96 L. Sun, Q. Shao, Y. Zhang, H. Jiang, S. Ge, S. Lou, J. Lin, J. Zhang, S. Wu and M. Dong, *J. Colloid Interface Sci.*, 2020, **565**, 142–155.

97 T. Ramachandran, R. K. Raji and M. D. Rezeq, *J. Mater. Chem. A*, 2025, **13**, 12855–12890.

98 B. Tahir, A. Alraeesi and M. Tahir, *Front. Chem.*, 2024, **12**, 1448700.

99 M. Cabrero-Antonino, A. Uscategui-Linares, R. Ramírez-Grau, P. García-Aznar, G. Sastre, J. Zhang, S. Goberna-Ferrón, J. Albero, J. Yu and H. García, *Angew. Chem., Int. Ed.*, 2025, e202503860.

100 A. Rajan, M. Daniel, J. Rafi, A. S. C. Lazuli and B. Neppolian, *ChemSusChem*, 2025, **18**, e202400207.

101 L. Shi, C. Wu, Y. Wang, Y. Dou, D. Yuan, H. Li, H. Huang, Y. Zhang, I. D. Gates and X. Sun, *Adv. Funct. Mater.*, 2022, **32**, 2202571.

102 V.-A. Thai, T.-B. Nguyen, C.-W. Chen, X.-T. Bui, R.-A. Doong and C.-D. Dong, *Environ. Sci.: Nano*, 2024, **11**, 3871–3886.

103 S. Zhang and C. Bie, *Rare Met.*, 2025, 1–4.

104 Y. Li, Y. Liu, Z. Wang, P. Wang, Z. Zheng, H. Cheng, Y. Dai and B. Huang, *Chem. Eng. J.*, 2021, **411**, 128446.

105 Y. Sun, M. Xie, H. Feng and H. Liu, *ChemPlusChem*, 2022, **87**, e202100553.

106 J.-H. Zhao, L.-W. Liu, K. Li, T. Li and F.-T. Liu, *CrystEngComm*, 2019, **21**, 2416–2421.

107 Y. Chen, H. Zhu, S.-Z. Kang, T. Zhang, L. Qin and X. Li, *J. Alloys Compd.*, 2023, **961**, 170929.

108 L. Biswal, S. P. Tripathy, S. Dash, S. Das, S. Subudhi and K. Parida, *Mater. Adv.*, 2024, **5**, 4452–4466.

109 H. Zhu, Y. Chen, T. Zhang, L. Qin, S.-Z. Kang and X. Li, *J. Solid State Chem.*, 2023, **327**, 124298.

110 M. J. Molaei, *Fuel*, 2024, **365**, 131159.

111 J. Ke, F. He, H. Wu, S. Lyu, J. Liu, B. Yang, Z. Li, Q. Zhang, J. Chen and L. Lei, *Nano-Micro Lett.*, 2021, **13**, 1–29.

112 T. Ramachandran, R. K. Raji, S. Palanisamy, N. Renuka and K. Karuppasamy, *J. Ind. Eng. Chem.*, 2025, **145**, 144–168.

113 A. M. Bogale, T. Ramachandran, M. E. Suk, B. B. Badassa, M. M. Solomon, J. He, A. Yusuf, R. K. Raji, B. A. Zenebe and N. K. Amare, *J. Phys. Chem. Solids*, 2025, 113079.

114 J. Wei, F. Hu, Y. Pan, C. Lv, L. Bian and Q. Ouyang, *Chem. Eng. J.*, 2024, **481**, 148793.

115 H. Hassan, K. Khan, S. Mumtaz, A. A. Rafi, A. M. Idris, A. Althobaiti and A. Mohammad, *J. Power Sources*, 2024, **623**, 235486.

116 B. Jia, H. Yang, L. Wang, Z. Zhao and X. Wu, *Appl. Surf. Sci.*, 2022, **602**, 154386.

117 X. Yang, Y. Tian, S. Li, Y.-P. Wu, Q. Zhang, D.-S. Li and S. Zhang, *J. Mater. Chem. A*, 2022, **10**, 12225–12234.

118 Y. Wang, Y. Liu, C. Wang, H. Liu, J. Zhang, J. Lin, J. Fan, T. Ding, J. E. Ryu and Z. Guo, *Eng. Sci.*, 2020, **9**, 50–59.

119 H. Hassan, E. Umar, M. W. Iqbal, H. Alrobei, A. M. Afzal, A. K. Alqorashi, T. Yaseen and M. A. Sunny, *Electrochim. Acta*, 2024, **489**, 144277.

120 J. Wang, J. Gong, H. Zhang, L. Lv, Y. Liu and Y. Dai, *J. Alloys Compd.*, 2021, **870**, 159466.

121 X. Zhang, S. Yang, W. Lu, D. Lei, Y. Tian, M. Guo, P. Mi, N. Qu and Y. Zhao, *J. Colloid Interface Sci.*, 2021, **592**, 95–102.

122 X. Yang, C. Xu, S. Li, Y.-P. Wu, X.-Q. Wu, Y.-M. Yin and D.-S. Li, *J. Colloid Interface Sci.*, 2022, **617**, 633–640.

123 L. Yue, L. Chen, X. Wang, D. Lu, W. Zhou, D. Shen, Q. Yang, S. Xiao and Y. Li, *Chem. Eng. J.*, 2023, **451**, 138687.

124 S. Li, Y. Wang, Y. Li, J. Xu, T. Li and T. Zhang, *Nanomaterials*, 2023, **13**, 610.

125 T. Kshetri, D. D. Khumujam, T. I. Singh, Y. S. Lee, N. H. Kim and J. H. Lee, *Chem. Eng. J.*, 2022, **437**, 135338.

126 Y. Wang, C. Shi, Y. Chen, D. Li, G. Wu, C. Wang and L. Guo, *Electrochim. Acta*, 2021, **376**, 138040.

127 J. Lu, J. Wang, J. Gong and C. Hu, *J. Mater. Sci.: Mater. Electron.*, 2022, **33**, 18922–18937.

128 M. Adil, A. G. Olabi, M. A. Abdelkareem, H. Alawadhi, A. Bahaa, K. ElSaid and C. Rodriguez, *J. Energy Storage*, 2023, **68**, 107817.